

Submillimeter-Scale Topography of the Lunar Regolith

Paul Helfenstein

Center for Radiophysics and Space Research, Cornell University, Ithaca, New York 14853-6801

E-mail: helfenstein@cuspi.tn.cornell.edu

and

Michael K. Shepard

Department of Geography and Earth Sciences, Bloomsburg University, Bloomsburg, Pennsylvania 17815

Received April 23, 1998; revised March 5, 1999

We have applied computer stereophotogrammetry to Apollo Lunar Surface Closeup Camera (ALSCC) pictures of the lunar surface to construct the first-ever digital topographic relief maps of undisturbed lunar soil over spatial scales from 85 μm to 8.5 cm. Using elevation histograms, fractal analysis, and Hapke's photometric roughness model we show that *Apollo 14* (Fra Mauro) Imbrium ejecta is rougher than average *Apollo 11* (Mare Tranquilitatis) and *Apollo 12* (Oceanus Procellarum) mare surfaces at submillimeter to decimeter size-scales. We confirm the early result of K. Lumme *et al.* (1985, *Earth Moon Planets* 33, 19–29) that the cumulative distribution of elevations for lunar soil is typically well described by Gaussian statistics. However, cumulative distributions are insensitive to asymmetries in the shapes of elevation histograms: Of 11 discrete elevation histograms we measured, about half exhibit significant deviations from Gaussian behavior. We also confirm Lumme *et al.*'s finding that the roughnesses of all lunar surfaces increase with decreasing size-scale. We further show that the scale dependence of roughness is well represented by fractal statistics. The rates of change of roughness with size scale, represented by fractal dimension D , are remarkably similar among terrains. After correcting for the contribution of large-scale roughness, our average value of $D = 2.31 \pm 0.06$ falls within the range $2.0 \leq D \leq 2.4$ reported from lunar radar studies. The amplitude of roughness, which we characterize with the rms slope angle at 1-mm scale, varies significantly among terrains. For lunar mare, the average rms slope angle is $16^\circ \pm 4^\circ$ and that for Fra Mauro regolith is $25^\circ \pm 1^\circ$. By comparison to radar data, we suggest that the roughness of Fra Mauro (Imbrium ejecta) regolith is similar to that of lunar highland terrains. We find that the Gaussian slope distribution assumed in B. W. Hapke's model (1984, *Icarus* 59, 41–59) adequately describes typical lunar regolith surfaces. A revised form of Hapke's equation that models realistic particle phase functions and the coherent backscatter opposition effect was fitted to disk-resolved lunar photometric observations and yields estimates of $\bar{\theta} = 27 \pm 1^\circ$ for highland and $\bar{\theta} = 24 \pm 1^\circ$ for mare regolith. These values of $\bar{\theta}$ as well as the implied relative highland : mare photometric roughness ratio are best matched in our elevation data by the cumulative contributions of surface topography covering all scales greater than 0.1 mm. Less

than 5% of the photometrically detected roughness of lunar regolith is contributed by surface relief at scales larger than 8 cm. This conclusion implies that values of $\bar{\theta}$ derived from whole-disk and disk-resolved photometry, respectively, may be taken to represent the same physical quantity. In addition, particulate samples used in goniophotometric measurements should not be assumed to be photometrically smooth (i.e., $\bar{\theta} = 0^\circ$), as is often done in laboratory applications of Hapke's photometric model. The predicted photometric roughness at size scales of 0.1 mm and less significantly exceed photometric estimates and suggests that there exists a measurable size scale below which topographic relief either is not photometrically detectable or is not represented in the Hapke model as macroscopic roughness. © 1999 Academic Press

Key Words: stereophotogrammetry; lunar regolith; photometry; Moon; Apollo.

1. INTRODUCTION

The Apollo Lunar Surface Closeup Camera (ALSCC), shown in Fig. 1, is a 35-mm stereo format photographic instrument that was used by Apollo astronauts on the lunar surface nearly three decades ago (Gold 1970, Anderson 1971, Anderson and Nicksch 1971). Each photograph provided stereoscopic coverage of a 7×8 cm area of lunar soil at very high spatial resolution (85 μm at the surface). The complete collection of ALSCC images is presented in a series of preliminary science analyses (Gold 1969, 1970, 1971; Gold *et al.* 1970). Relatively little quantitative use has been made of these pictures despite the fact that, to date, they represent our best *in situ* observations of undisturbed lunar regolith texture and topography at submillimeter to subdecimeter scales. ALSCC images of astronaut bootprints and tire tracks left from the Modularized Equipment Transporter (MET; see Fig. 3) were used to investigate lunar soil mechanics (cf. Mitchell *et al.* 1971). A specially designed sequence of *Apollo 14* ALSCC images was used to support the Thermal Degradation Samples (TDS) experiment which tested the effects of lunar

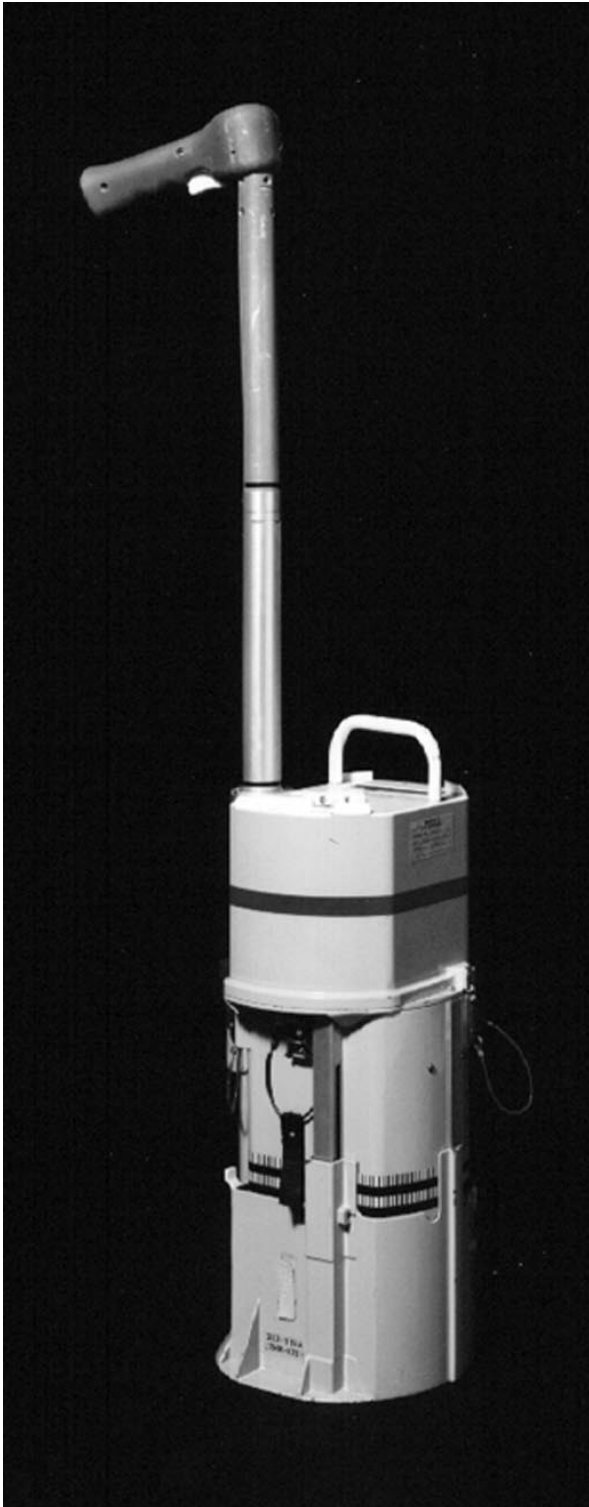


FIG. 1. Apollo Lunar Surface Closeup Camera (ALSCC). The stereo optics are contained in the upper portion of the camera base along with a 100-exposure magazine of high-definition 35-mm slide film. An internal flashbulb illuminated the target surface. The camera was operated by placing the camera base on target surface and depressing the trigger on the handle to expose the film.

dust on candidate thermal coatings for future space hardware. Shoemaker *et al.* (1970) studied the size-frequency distribution of fragmental material in *Apollo 12* soil by carefully analyzing a single ALSCC image (AS12-57-8451). More recently, Lumme *et al.* (1985) performed optical stereophotogrammetry on three ALSCC stereo pairs (*Apollo 11*, AS11-45-6702 and AS11-45-6707; and *Apollo 12*, AS12-57-8455) to extract and analyze several topographic profiles. Their results showed that regolith surface roughness, as measured by average rms slope angles, monotonically increases with decreasing size scale and that the cumulative distribution of elevations is typically Gaussian.

In this study, we apply computer stereophotogrammetry to construct digital topographic maps from the subset of the Apollo closeup stereo pairs that best represent the texture of undisturbed lunar soils. Our main purpose is to produce a topographic data base to be used as “ground truth” for the testing and improvement of radiative transfer models that are used to measure planetary surface roughness from remotely sensed data such as radar observations, optical polarimetry, and photometry. The topographic maps also provide fundamental geological information about the textural similarities and differences among a variety of lunar soil types. Using them, we expand considerably the early effort of Lumme *et al.* (1985). For example, while Lumme *et al.* (1985) extracted 1400 elevation measurements from 3 stereo pairs, we will make use of 11 stereo pairs to collect over 9 million elevation measurements. We will also extend the analysis to *Apollo 14* images (excluded by Lumme *et al.*). We compare a variety of different lunar surfaces in terms of roughness variations as measured by elevation histograms, fractal statistics, and Hapke’s (1984) macroscopic roughness parameter.

2. IMAGE SELECTION

The ALSCC was used on only three Apollo flights (*11*, *12*, and *14*) from which a total of 48 stereo pictures were returned (17 from *Apollo 11*, 15 from *Apollo 12*, and 16 from *Apollo 14*). Only about a third of the pictures show examples of undisturbed lunar soil or rock surfaces of which 11 were selected for the present study (Table II). We excluded from the analysis pictures which show lunar soil that was disturbed by rocket exhaust or that was extensively covered by granular “foot spray” particles kicked up by the astronauts’ boots, and pictures showing lunar soil that was intentionally disturbed to demonstrate its cohesive properties.

Our selection (Table II; Fig. 2) consists of three pictures from *Apollo 11* (Mare Tranquilitatis), four from *Apollo 12* (Oceanus Procellarum), and four from *Apollo 14* (Fra Mauro). At least two frames from each mission (AS11-45-6699/6701; AS12-57-8449/8453; AS14-77-10368/10370) represent typical examples of undisturbed lunar soil. A few less-common surfaces are also pictured. These include two examples of soil-covered rocky surfaces (AS14-77-10371/72), clumpy regolith on the inside of a crater (AS12-57-8454), and glass-coated regolith clumps (AS11-45-6704) and stones (AS12-57-8452). *Apollo 11* and

12 examples are considered to represent lunar mare regolith, while *Apollo 14* soils (Fra Mauro) are interpreted as Imbrium basin ejecta. None of our independently selected stereo pairs match those chosen by Lumme *et al.* (1985) listed earlier. We excluded AS11-45-6702 because it showed a pattern that gave the appearance of aerodynamic erosion and scouring by rocket exhaust could not be ruled out (Gold 1970). Our selection of *Apollo 12* picture AS12-57-8454 shows an unusual clumpy soil inside an impact crater which is remarkably like clumpy soil in an open area seen in Lumme *et al.*'s AS12-57-8455. We chose the former over the latter because the 8454 frame is known to have originated inside a crater, whereas 8455 is *hypothesized* to be impact ejecta (Gold 1970, Gold *et al.* 1970). Finally, while AS11-45-6707 was one of our candidate images, we noticed more extensive deposits of relatively coarse particles (reminiscent of footspray contamination) than in images which Gold (1970) classified as "undisturbed soil."

The exact locations on the lunar surface where most the ALSCC pictures were acquired cannot be determined with great confidence. All *Apollo 11* ALSCC pictures were obtained within 15 m of the lunar module; however, because of the small size of the camera footprint, the specific targets cannot be identified within the large-scale lunar surface photography (Gold 1969). *Apollo 12* ALSCC pictures were obtained on the north side and within 70 m of the lunar module. However, the 5 minutes of time available to expose the 15 stereo pairs was insufficient to allow astronauts to properly orient the camera and document the targets and their locations (Bean *et al.* 1970). We are able to identify the locations of the *Apollo 14* (Fra Mauro) images used in this study. They were obtained at Geology Station A, 180 m ENE from the lunar module. The pictures were taken on and in the vicinity of "sloping rock," a gently sloping rocky surface that is seen in *Apollo 14* Hassellblad picture AS14-68-9409 (Fig. 3) from a distance of about 15 m (Swann *et al.* 1971).

3. STEREOGRAMMETRY

Stereophotogrammetry relies on the measurements of parallax offsets between individual features visible in both left- and right-side frames of a stereo pair. Each ALSCC stereo pair consists of a separate left- and right-side 35-mm color slide transparency. We enlarged and digitally scanned each stereo half-frame into a byte-format data array with pixel dimensions large enough to oversample the limiting spatial resolution by 25%.

We developed our own computer software for automated, pixel-by-pixel measurements of parallax offsets. While computer software for stereophotogrammetry is now widely available, the packages we examined prior to developing our own are interactive programs that rely on manual or computer-aided identification of individual tiepoints followed by resampling and interpolation of a large number of intermediate points to form a rectangular grid of parallax offsets. The most reliable approach employed two-dimensional Fourier autocorrelation methods to match brightness patterns contained in a small square subsection

(correlation window) extracted from each half of a stereo pair. None of the pattern-matching algorithms attempted to adjust the brightness patterns within correlation windows to account for relative foreshortening (or stretching) of the brightness patterns that accompany planar projection of three-dimensional features from the two different viewpoints. In addition, the correlations corresponding to each tiepoint were not used as statistical weights in performing the interpolation of intermediate points, and no provision was made for measuring and correcting any possible misalignment of the stereo frames.

Our feature-matching program was developed from subpixel-precision image-coregistration software and measures pixel offsets in the line (y) as well sample (x) directions to account for the fact that slight rotations and offsets may have been introduced when we digitally scanned the separate half of each stereo pair. We have developed a two-stage, iterative approach that adjusts correlation windows for relative foreshortening, makes use of correlation coefficients to interpolate poorly correlated regions of the offset map from surrounding pixels that are well correlated, and measures offsets to subpixel precision.

The left half of each stereo pair is adopted as the geometric reference frame and stereo offsets (pixel displacement vectors) are measured to features in the right frame. The displacement search is performed pixel by pixel. For any given pixel location in the left image, a rectangular correlation window centered on that pixel location is defined. To overcome ambiguity that results when bland (featureless) areas of a scene are encountered, the size of the correlation window is automatically adjusted until the maximum contrast of pixel brightness values within the window exceeds a threshold contrast value (usually 15–25% for ALSCC images). Next, a correlation window of the same size is extracted from the right image at a location centered on a trial position which is incrementally changed until the linear correlation in pixel brightness values between the left and right correlation windows is maximized. Even on modern computer workstations, it is impractical to search a large range of trial offsets at full spatial resolution. To streamline the speed of the search process, each stereo pair is first reduced to 1/5 its original size and a 1/5-scale offset vector map is constructed along with a corresponding map of pixel-by-pixel correlation coefficients. The correlation map is used to identify areas where displacement vectors for poorly correlated features must be interpolated from vectors for surrounding well-correlated features. It also provides statistical weights for performing the interpolations. The low-resolution stereo pairs and their corresponding parallax offset maps are incrementally resized to higher resolution where they are used as first approximations in subsequent measurements at increasingly higher precision levels. The process is repeated until it converges on full-scale offsets measured to 1/16 pixel precision.

During the first stage of the parallax measurements, no attempt is made to adjust for rotation and offset distortions introduced during digital scanning and for foreshortening of features within correlation windows due to planar projection of three-dimensional surfaces from different viewpoints. However,

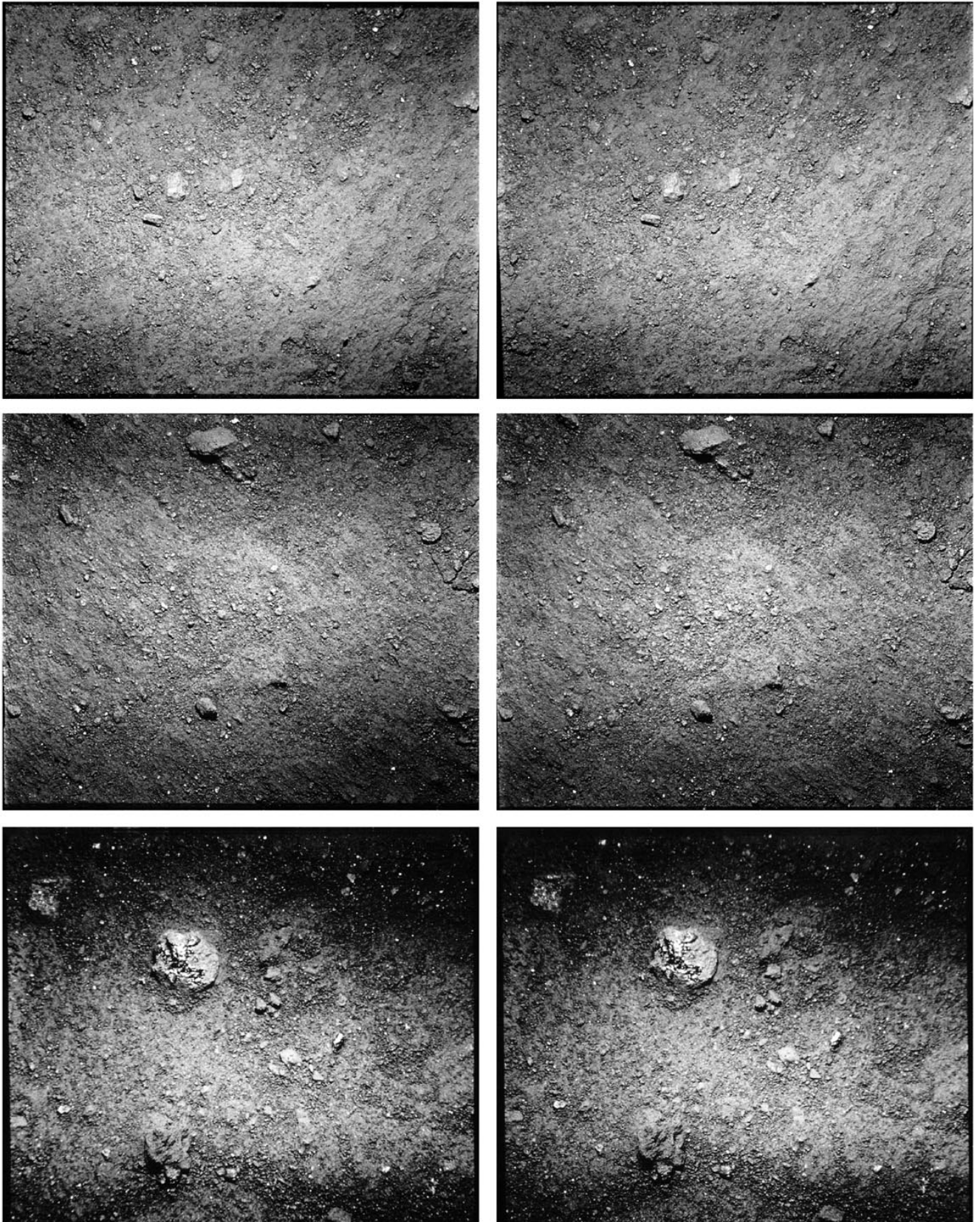


FIG. 2. Stereo images selected for this study. (a) *Apollo 11* images: AS11-45-6699 (top), AS11-45-6701 (middle), AS11-45-6704 (bottom); (b) *Apollo 12* images: AS12-57-8449 (top), AS12-57-8452 (middle), AS12-57-8453 (bottom); (c) *Apollo 12* image AS12-57-8454 (top), *Apollo 14* images AS14-77-10368 (middle) and AS14-77-10370 (bottom); (d) *Apollo 14* images of soil-covered rock: AS14-77-10371 (top), AS14-77-10372 (bottom).

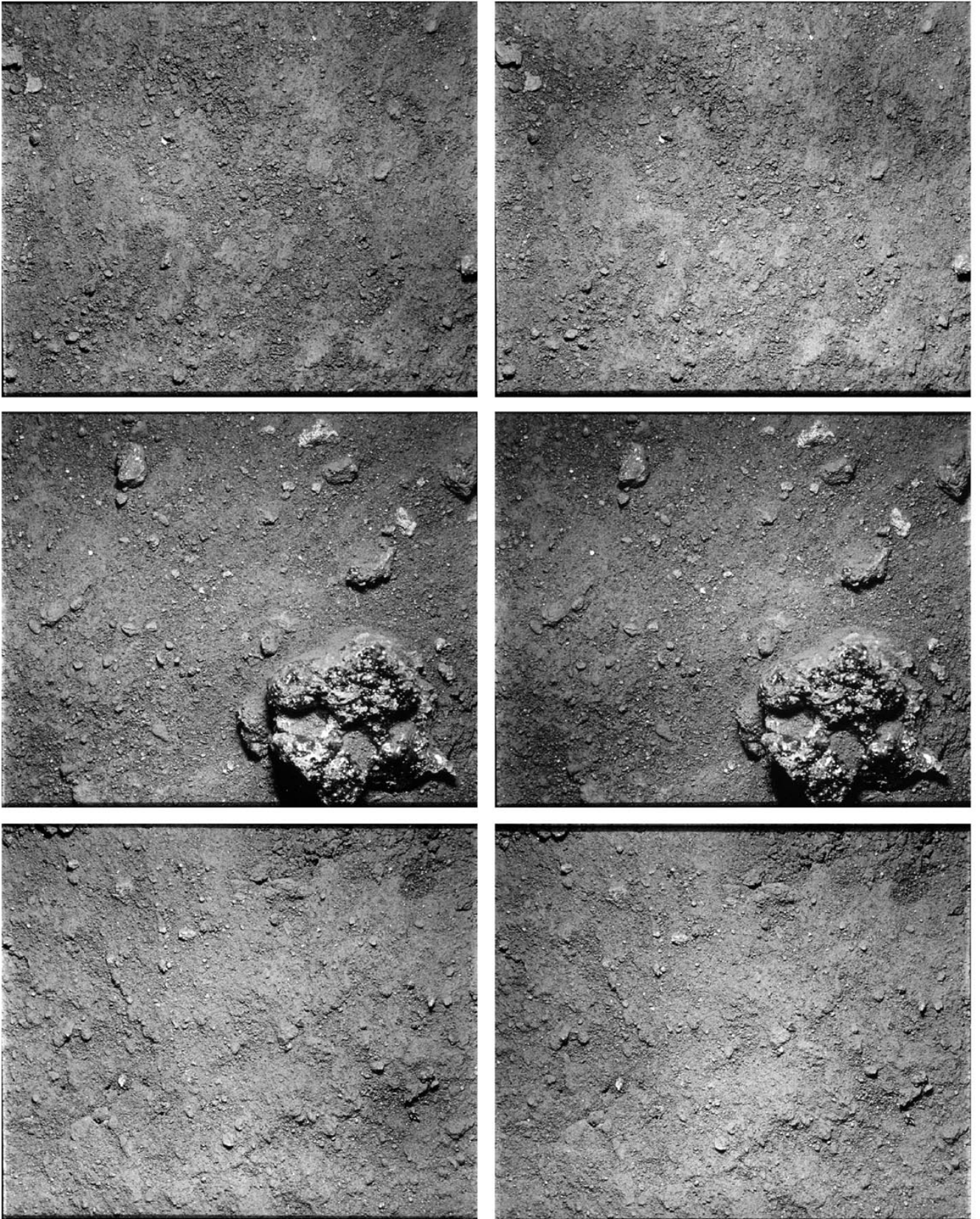


FIG. 2—Continued

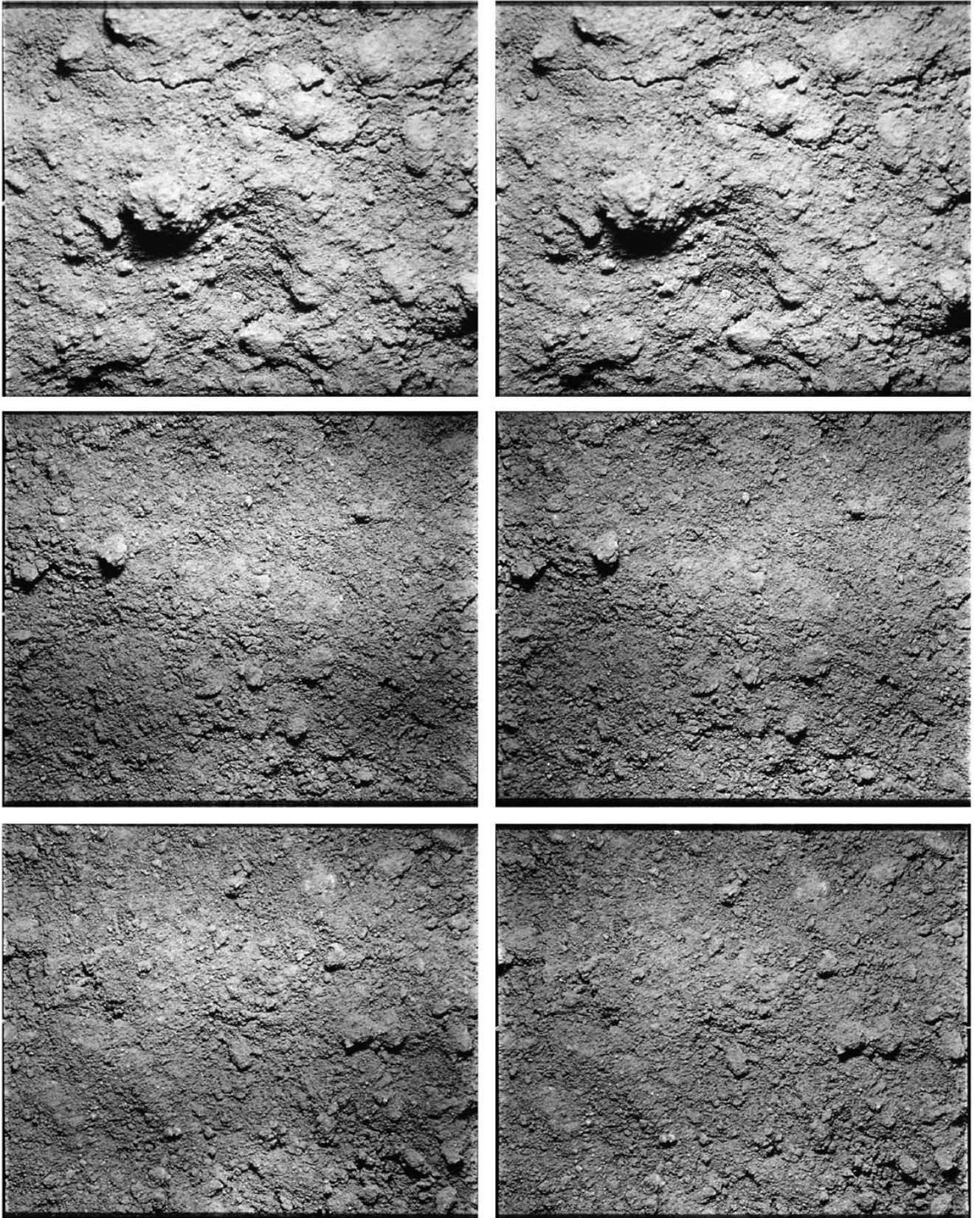


FIG. 2—Continued

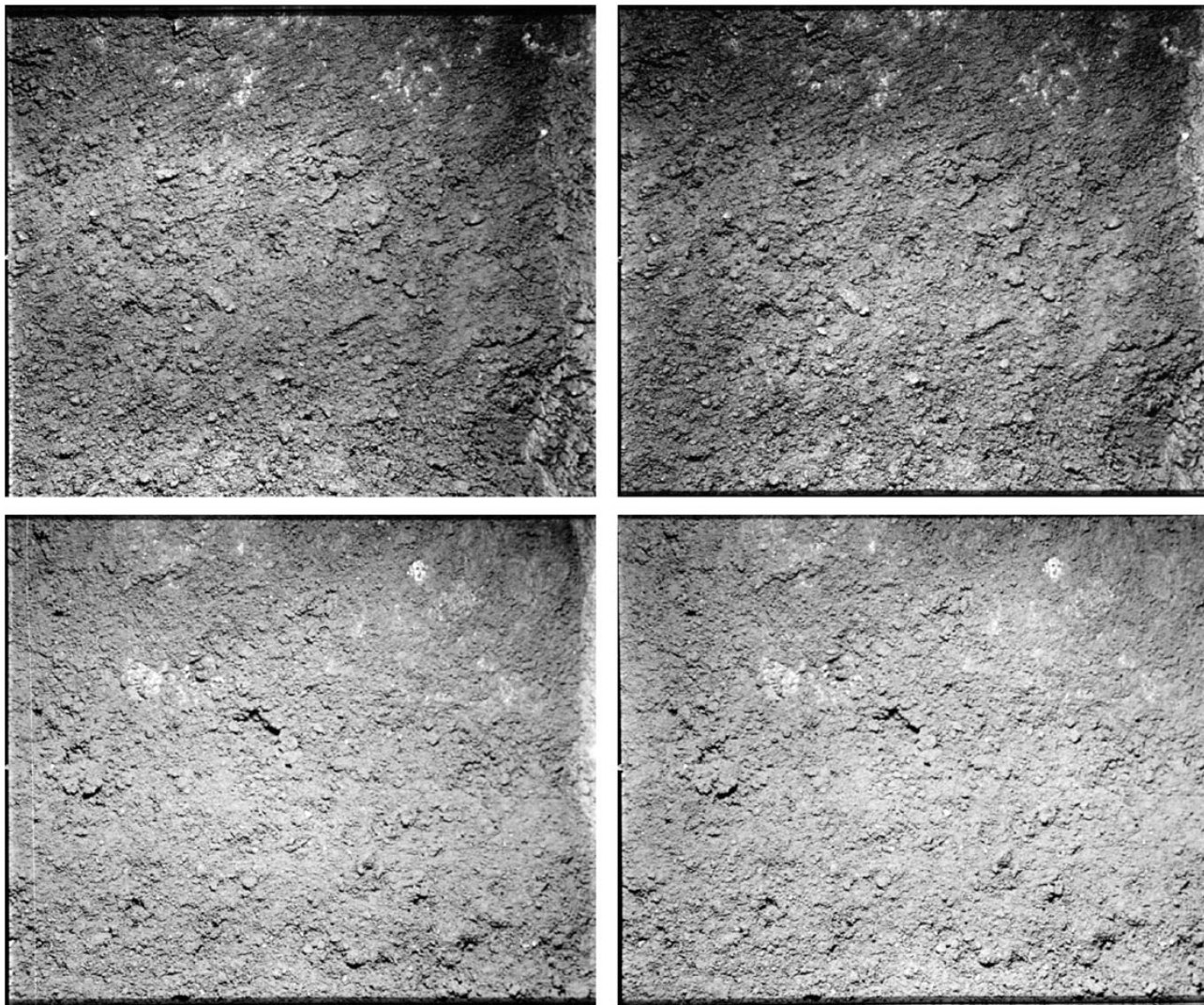


FIG. 2—Continued

accurate parallax offsets can be derived only if these distortions are iteratively corrected during the pattern-matching process. Thus, the second stage of displacement measurement applies the first-stage results to remap and reduce distortions of features in the right image so that they better match corresponding features in the left (reference) images. The distortion corrections are iteratively improved as the second-stage search progresses to increasingly higher levels of accuracy.

The camera geometry data needed to compute elevations from corresponding parallax offsets is given in Table I. The elevation map coordinate system (X_e , Y_e , Z_e) has its origin at the base of the camera assembly, centered at the midpoint separating the two lenses of the stereo camera. We define separate Cartesian coordinate systems, respectively, for the left (x_L , y_L) and right (x_R , y_R) image component of each stereo pair, with the positive x directions of each system increasing in exactly opposite directions away from the origin of the elevation system. The origin

TABLE I
Relevant Facts about the Apollo Lunar Surface
Closeup Camera (ALSCC)

Film	Kodak Ektachrome MS (SO-368) 35-mm color reversal film
Magnification	0.33 \times
Parallax angle	9 $^\circ$
Horizontal spatial resolution	85 μ m
Footprint	72 \times 82.8 mm
Base-to-height ratio	0.16
Optics	Kodak M-39 diffraction-limited copy lenses f/17 full aperture stopped down to f/22.6 Focal length: 46.12 mm Focal plane distance (f_p): 64.065 mm Focus (H): Fixed at 187.065 mm Lens separation (D): 29.0 mm

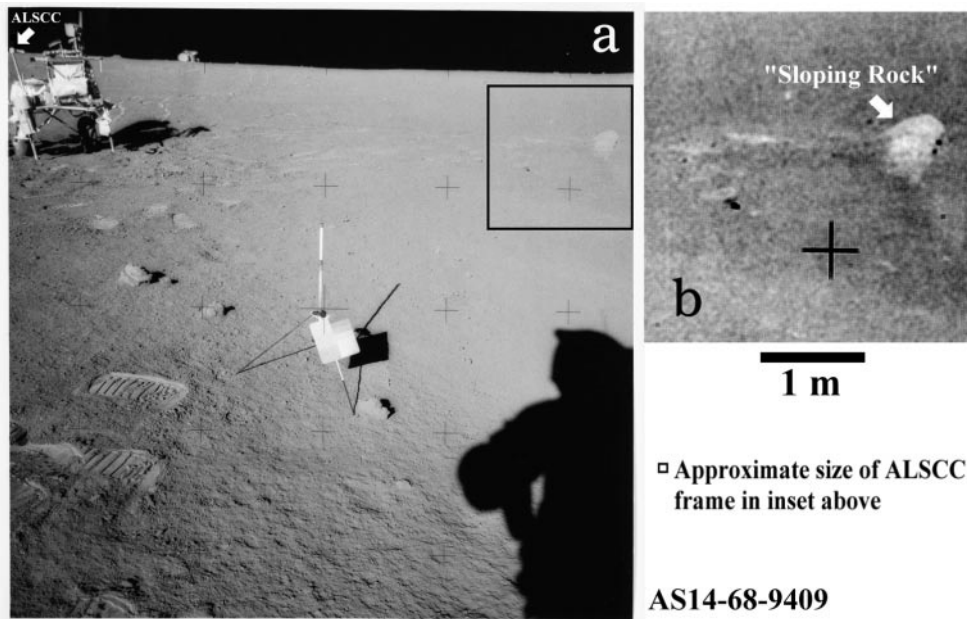


FIG. 3. Location where *Apollo 14* ALSCC images used in this study were photographed. (a) *Apollo 14* Hasselblad image AS14-68-9709. The ALSCC is seen in its stowed position on the Modular Equipment Transporter (MET) at the far left (arrow). The lunar module is visible on the horizon (left of center). Square outline at right highlights the location of “sloping rock” shown in greater detail in inset. (b) Enlargement of outlined section in (a). Features have been contrast enhanced to show details. Arrow points to “sloping rock” where ALSCC images AS14-77-1037/10372 were obtained. Scalebar refers to (b). Also shown is the approximate projected footprint size of an ALSCC frame.

of each frame’s coordinate system is its principal point (i.e., the nadir projection of the optical axis onto the plane of the camera base). To optimize the stereo overlap between left and right frames of each stereo pair, the ALSCC was designed so that the principal points are 4.97 ± 0.02 mm to either side of center of each frame as measured in the film plane. Due to parallax, a surface feature with nonzero elevation is projected onto the right image plane as foreshortened (or stretched) in the x direction relative to its counterpart in the left image plane. The elevation, Z_e , of any such feature relative to datum, H (the vertical distance of the lens plane from the camera base), is computed from the parallax offset, $x_R - x_L$ as

$$Z_e = H - \frac{f_p D}{x_R - x_L}, \quad (1a)$$

where f_p is the distance of the focal plane from the lens, and D is the lens separation distance. Because we measured parallax offsets relative to the left frame of reference, the horizontal elevation map coordinates (X_e , Y_e) are evaluated from left-frame coordinates using

$$X_e = \frac{x_L}{f_p}(H - Z_e) - \frac{D}{2} \quad \text{and} \quad Y_e = \frac{y_L}{f_p}(H - Z_e). \quad (1b, 1c)$$

When the stereo pair is properly aligned for stereo viewing, the principal points define a single line that is coincident with the x axes of the two frame-coordinate systems and parallax

offsets occur only in the x direction (i.e., $y_R - y_L = 0$). Prior to applying Eqs. (1), we correct for any misalignment of the left and right frames by searching for whole-frame rotation and offsets that minimize the sum of squares of $y_R - y_L$. Also, because we originally scanned the images with 25% oversampling, we resize and renormalize the offset maps to proper scale at this stage.

We adopted the above approach to construct 11 raw elevation maps that have horizontal spatial resolution of $85 \mu\text{m}/\text{pixel}$ and a nominal vertical resolution of $50 \mu\text{m}$. In our raw elevation maps, mean elevations (Table II) were found to deviate slightly (usually less than 1 mm) from the camera base datum. In some cases it was evident that the astronauts positioned the camera base somewhat above the lunar surface, apparently to avoid disturbing the soil. To correct for differences in the camera placement, we renormalized each digital elevation map relative to the mean reported in Table II. All 11 elevation maps are presented in Fig. 4. The maps show elevations ranging from -2.5 to $+2.5$ cm. It is clear from direct examination of the maps that at subdecimeter scales, undisturbed lunar mare are typically smoother than undisturbed Fra Mauro (Imbrium ejecta) soils—an inference that we explore in detail below.

4. MEASUREMENTS OF SURFACE ROUGHNESS

In this section, we compare the surface roughness of different lunar soils as measured by three different methods: elevation histograms, fractal analysis, and Hapke’s (1984) photometric

TABLE II
Apollo Stereo Images Used in this Study

Frame number	Description	Elevation map normalization data		
		Mean elevation (mm)	Local slope angle/azimuth ^a	
AS11-45-6699	Undisturbed mare soil	0.129	0.5°	-117.7°
AS11-45-6701	Undisturbed soil with trace amounts of footspray	-0.328	4.6°	-73.1°
AS11-45-6704	Undisturbed mare soil with glazed regolith clumps	0.053	1.1°	-104.4°
AS12-57-8449	Undisturbed soil with striation of unknown origin	0.667	2.1°	+108.5°
AS12-57-8452	Undisturbed soil and glazed pebble inside a crater	5.213	4.4°	+144.8°
AS12-57-8453	Undisturbed soil with minor contamination by footspray (lower edge)	-0.19	3.3°	+105.0°
AS12-57-8454	Undisturbed clumpy regolith inside a crater	-0.221	8.3°	-91.1°
AS14-77-10368	Undisturbed soil	-0.101	4.2°	-100.3°
AS14-77-10370	Undisturbed soil	0.547	6.8°	+99.7°
AS14-77-10371	Soil-covered rock surface	-2.074	2.2°	+63.9°
AS14-77-10372	Soil-covered rock surface	-2.427	3.2°	-53.3°

^a The tilt azimuth of the upward-facing surface normal as determined from the best-fit plane is measured positive in the counterclockwise direction from right in the elevation map frames.

roughness model. The elevation maps in Fig. 4 show lunar surface relief superposed on an overall local slope (either a real topographic slope or an apparent one due to nonvertical pointing of the camera). To remove the local tilt from each map and represent elevations relative to a flat datum, we resampled the elevations relative to their distance from the best-fit (least-squares) plane covering the footprint area. The slope angles and tilt azimuths of the least-squares planes are given in Table II. Tilt corrections ranged from 0.5° to 8.3° but averaged about 3.7°. Even the tilt corrections themselves provide some information on the subdecimeter-scale roughnesses of different soils. For example, the rms tilt correction for our undisturbed Fra Mauro regolith ($5.7^\circ \pm 1.3^\circ$) is more than a factor of 2 larger than the average from five examples of undisturbed mare ($2.8^\circ \pm 1.5^\circ$).

Figure 5 provides a topographic profile extracted from each image. We have arranged them such that profiles with relatively large relief are at the top and examples with relatively small relief are at the bottom. Profiles a and b are examples of soil on rock in which some of the rock is exposed. Profiles c–g are typical profiles from lunar mare. To give some idea of the visible range of topography, we chose profiles that traversed relatively large stones in profiles e and f. Typical examples of Fra Mauro regolith are shown in profiles h and i. Profile j is a profile passing through a large stone at the bottom of a mare crater, and profile k shows the unusually fluffy clumps of regolith found on the inside of a mare crater. At the smallest scales that can be seen (approximately submillimeter scales), nearly all terrains

(with the possible exception of profile k) appear to have similar fine-scale textures. At least to visual inspection, the primary difference among the profiles appears to be in the contribution of larger-scale (approximately centimeter and larger scales) texture.

4.1. Elevation Statistics

Two alternate methods for describing the statistical distribution of elevations are elevation histograms and cumulative distributions of elevations, respectively. Lumme *et al.* (1985) studied cumulative distributions of elevations from several ALSCC topographic profiles and concluded that lunar soil topography obeys Gaussian statistics at subdecimeter scales. However, they did not test their conclusion against discrete elevation histograms corresponding to individual ALSCC images. In Fig. 6, we examine our data both in terms of elevation histograms (Fig. 6a) and cumulative distributions of elevation (Fig. 6b).

Elevation histograms (Fig. 6a) were sampled in horizontal resolution increments of 0.085 mm and binned in 0.1-mm increments of elevation. Most of the histograms are unimodal, although multimodal examples are evident in cases where significant portions of the frames are covered with large stones (AS12-45-8452), soil-covered rock (AS14-77-10372), or contamination from footspray (AS12-45-8453). The most notable systematic differences among terrains are that the narrowest histograms (AS11-45-6699, -6701, -6704, and AS12-57-8449 in Fig. 6a) occur for undisturbed lunar mare, while the broadest

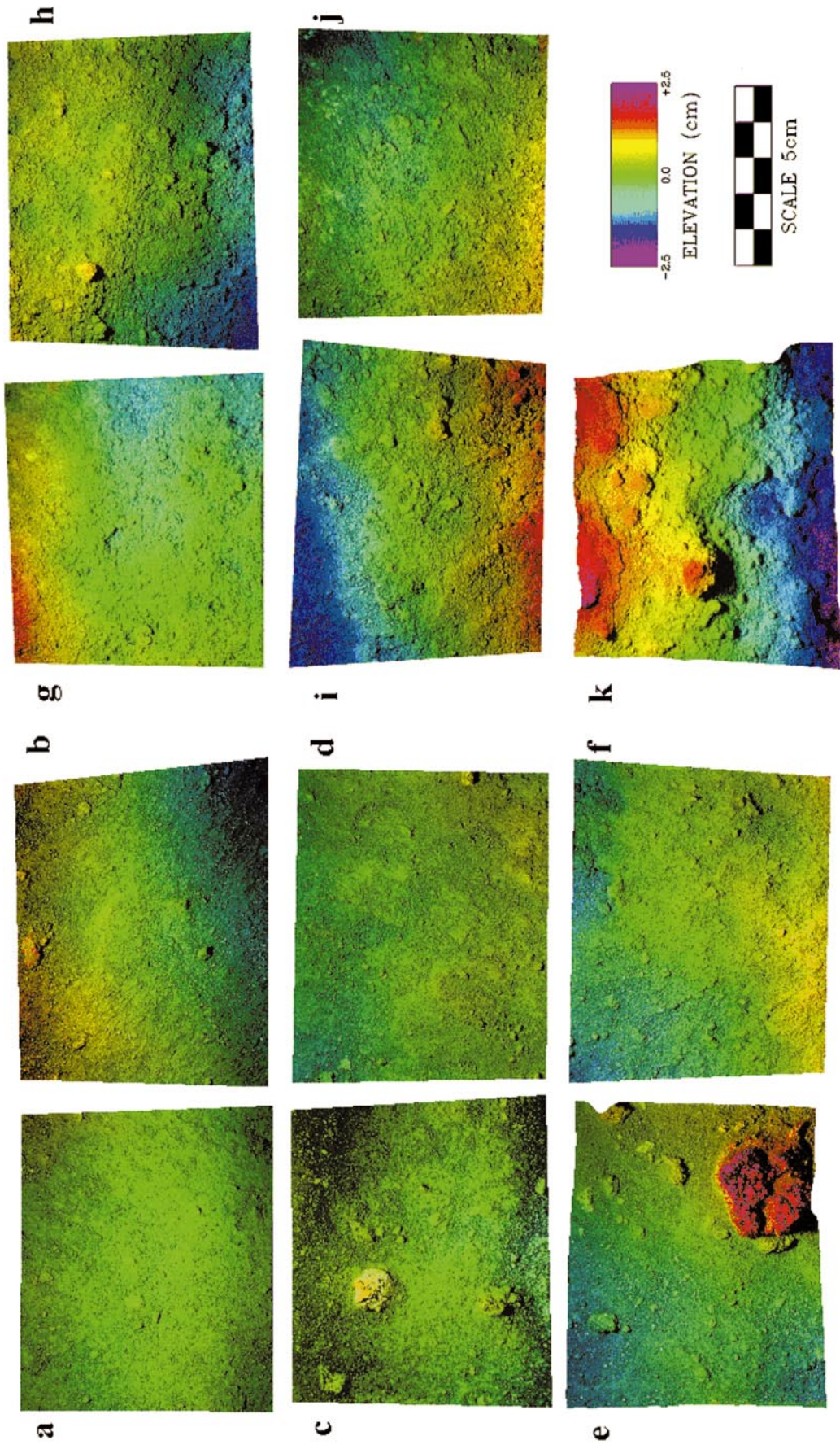


FIG. 4. Elevation maps derived from ALSCC images: (a) AS11-45-6701, (b) AS11-45-6699, (c) AS11-45-6701, (d) AS12-57-8449, (e) AS12-57-8452, (f) AS12-57-8453, (g) AS14-77-10368, (h) AS14-77-10370, (i) AS14-77-10371, (j) AS14-77-10372, (k) AS12-57-8454.

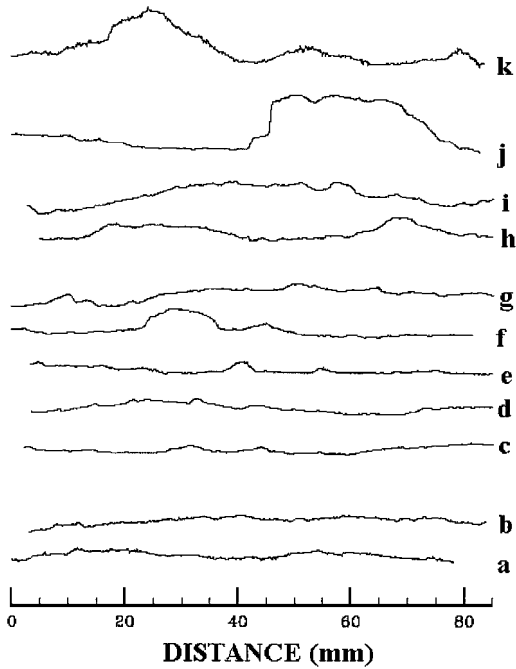


FIG. 5. Elevation profiles extracted from each of the elevation maps (no vertical exaggeration). At the bottom (a,b) are two soil-covered rock surfaces. Immediately above are five examples of lunar mare soils (c–g). Two lunar highland soils are represented in (h) and (i). Profile (j) is across a large stone at the bottom of an *Apollo 12* crater. Profile (k) represents unusual, fluffy regolith inside an *Apollo 12* crater.

occur in undisturbed Fra Mauro regoliths (AS14-77-10368) and the unusual clumpy regolith that was found inside a crater at the *Apollo 12* landing site (AS12-57-8454).

The elevation histograms were analyzed (Table III) in terms of standard deviation about the mean (σ), skewness (skew), and kurtosis (kurt). Skewness is a measure of the deviation of the shape of the distributions from symmetric. For a Gaussian (symmetric) distribution, skew = 0. Kurtosis measures the

peakedness of the distribution and is equal to 3 for a Gaussian distribution (cf. Chou 1972). Distributions with kurtosis values less than 3 (mesokurtic distributions) are more strongly peaked than Gaussian, and those with kurtosis values greater than 3 (platykurtic distributions) are broader than Gaussian forms. Table III shows that the average range of elevations, characterized by σ , is narrower for typical mare (*Apollo 11*, 1.08 ± 0.04 mm and *Apollo 12*, 1.35 ± 0.64 mm) than for undisturbed Fra Mauro regolith (*Apollo 14*, 1.95 ± 0.49 mm), consistent with the interpretation that maria are smoother than Fra Mauro soils even at these small scales. Broad elevation histograms (relatively large σ and kurtosis) occur when large (centimeter-scale) isolated stones or fluffy clods of regolith are present. There is no obvious systematic relationship between skewness and regolith type; however, nonzero values of skew indicate that the height distributions exhibit significant non-Gaussian behavior in about half of the cases studied. To better illustrate the extent to which individual histograms in Fig. 6a are well represented by Gaussian distributions, we have plotted the corresponding Gaussian distribution functions

$$f_G(h) = \frac{1}{\sqrt{2\pi}\sigma} \exp\left(-\frac{1}{2}\left[\frac{h}{\sigma}\right]^2\right), \quad (2)$$

where height is represented as h and σ is the standard deviation from Table III.

The cumulative distribution gives the fraction of total points whose heights lie in the interval $-h/\sigma \leq y \leq +h/\sigma$, and can be measured by direct numerical integration of the histograms in Fig. 6a. An obvious shortcoming of a cumulative distribution is that information about the asymmetry (skewness) of the histogram is lost by integrating from the negative to positive range of h/σ . Consequently, it is possible for many different types of statistical distributions to approximate Gaussian behavior when represented in cumulative distribution form. In Fig. 6b, cumulative distributions of elevation are represented as solid lines. The

TABLE III
Elevation Histogram Analysis of Apollo Closeup Elevation Maps

Picture frame	Elevation histogram			Modality	Comment
	σ (mm)	skew	kurt		
AS11-45-6699	1.1	+0.9	3.9	Unimodal	Nominal mare soil sample
AS11-45-6701	1.1	+0.4	4.1	Unimodal	Small stones present
AS11-45-6704	1.3	+1.3	6.2	Unimodal	Nominal mare soil sample
AS12-57-8449	0.9	+0.4	3.8	Unimodal	Nominal mare soil sample
AS12-57-8452	3.6	+1.3	4.8	Trimodal	Large stone present
AS12-57-8453	1.8	-0.2	2.1	Bimodal	Nominal mare soil sample
AS12-57-8454	2.6	+0.7	6.3	Unimodal	Unusual fluffy regolith inside crater
AS14-77-10368	2.3	-0.1	2.4	Bimodal	Nominal Fra Mauro soil sample
AS14-77-10370	1.6	-0.2	3.1	Unimodal	Nominal Fra Mauro soil sample
AS14-77-10371	1.5	+0.7	4.7	Unimodal	Soil-covered rock
AS14-77-10372	2.3	-0.1	2.2	Bimodal	Contact of rock with soil fillet

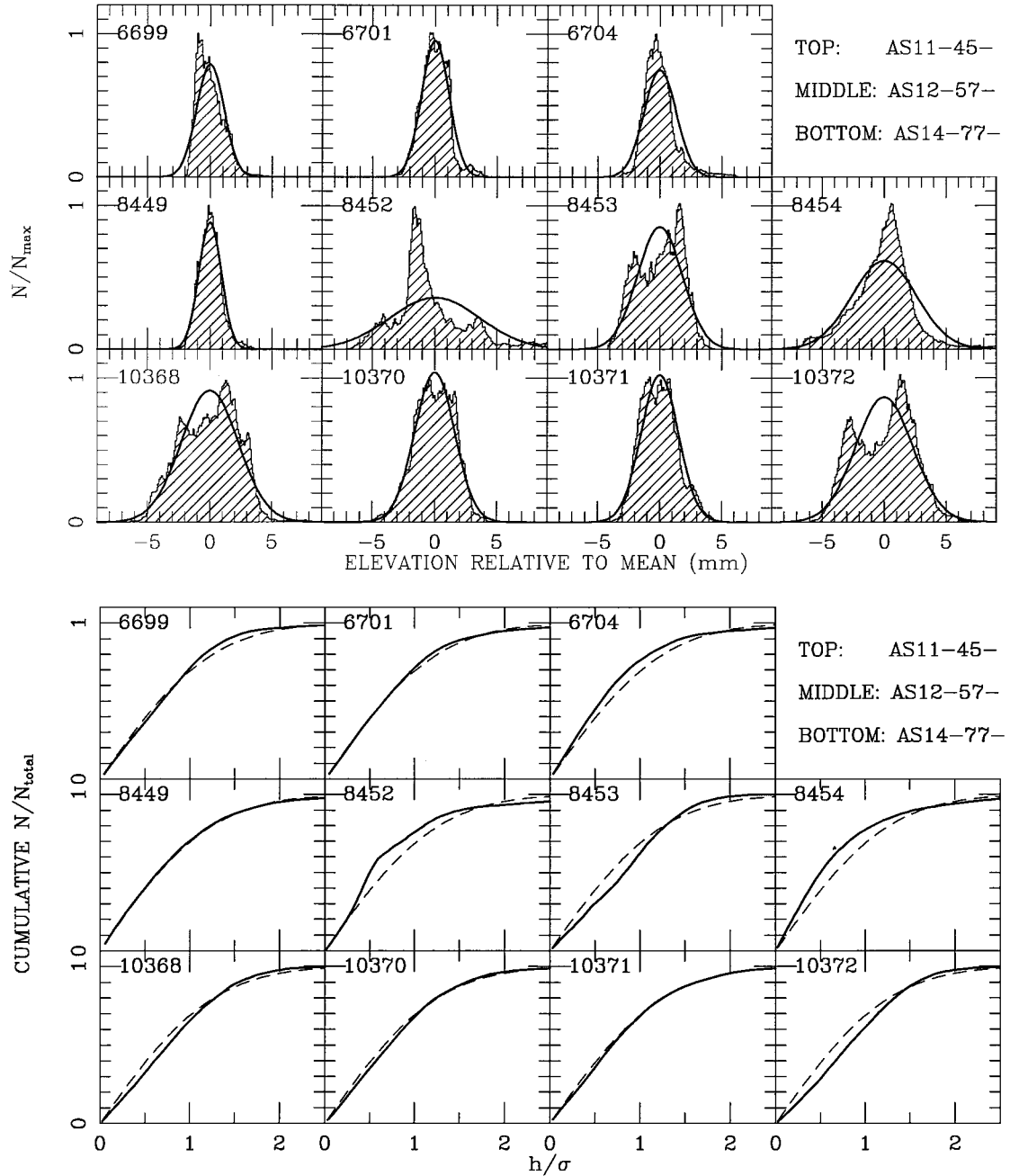


FIG. 6. (a) Elevation histograms derived after removing local topographic gradient (see text). Data were sampled in horizontal resolution increments of 0.085 mm and have been binned in 0.1-mm increments of elevation. Top row is *Apollo 11*, middle row *Apollo 12*, and bottom row *Apollo 14* examples. Solid line shows the Gaussian distribution corresponding to the sample standard deviation about the mean. N/N_{\max} is the number of samples normalized relative to the maximum number per bin. (b) Cumulative distributions of elevation corresponding to the elevation histograms in (a). Solid lines represent the results of directly integrating the elevation histograms. Dashed lines show the cumulative Gaussian distribution (Lumme *et al.* 1985).

corresponding cumulative Gaussian distribution (Lumme *et al.* 1985), $F_G(y)$, for each is derived by integrating over $f_G(h)$:

$$F_G(y) = 2 \int_{-\infty}^y f_G(h) dh - 1. \quad (3)$$

Cumulative Gaussian distributions are plotted as dashed lines

in Fig. 6b. While Figure 6b supports Lumme *et al.*'s conclusion that the cumulative distribution of elevations for lunar regolith are generally Gaussian; comparison to Fig. 6a demonstrates that *cumulative distributions* do not provide a very sensitive measure of the true shape of elevation histograms—about half of the elevation histograms exhibit non-Gaussian shape asymmetries.

4.2. Fractal Analysis

A significant body of work has established that the topographic roughness of naturally occurring geological surfaces, as measured by mean slopes, changes with the length scale used in its measure. Fractal analysis (cf. Kaye 1978, Orford and Whalley 1983, Mark and Aronson 1984, Power and Tullis 1991, Turcotte 1992, Chase 1992, Shepard *et al.* 1995) has become a popular quantitative method for characterizing both the rate of change of roughness with spatial scale and the amplitude of roughness. Fractal descriptions of surface roughness have recently been introduced to remote-sensing models (Shepard *et al.* 1995, Shkuratov 1995, Campbell and Shepard 1996, Shepard and Campbell 1998). Natural topography is best characterized by self-affine fractal measures. Self-affinity is the property of surface topography to scale more slowly in the vertical direction than in the horizontal direction, with a rate characterized by the fractal dimension D , where $2 \leq D \leq 3$. Surfaces with small D are visually perceived as retaining their roughness as the size scale increases, while those with large D appear to smooth quickly as scale is increased. The amplitude of roughness is characterized by the rms slope angle at a unit reference scale (in this study, at 1-mm scale).

We explore the fractal behavior of lunar soil relief by applying the variogram method (Mark and Aronson 1984, Chase 1992) to analyze our digital topographic maps from which the regional tilt has been removed. In this method, the mean Allan variance (Allan 1966),

$$\bar{v}_A^2 = \frac{1}{N} \sum_{j=1}^N [z(x_j + \Delta x) - z(x_j)]^2, \quad (4)$$

is measured as a function of size scale Δx , where z is elevation and the mean is obtained by summing over all horizontal locations, x_j . A surface exhibits fractal behavior over the domain of scales for which a single power law relates the mean Allan variance to size scale

$$\bar{v}_A^2 = v_{\text{ref}}^2 \Delta x^{2H}, \quad (5)$$

where the coefficient v_{ref}^2 is the Allan variance at a unit reference scale (i.e., at $\Delta x = 1$ mm) and H is known as the Hurst exponent. The surface fractal dimension is related to the Hurst exponent by $D = 3 - H$. The rms slope angle at unit reference scale, Θ_{RMS} , can be evaluated from

$$\tan(\Theta_{\text{RMS}}) = \sqrt{v_{\text{ref}}^2}. \quad (6)$$

A variogram plot (i.e., a log-log plot of Allan variance as a function of corresponding size scale) for each of our elevation maps is provided in Fig. 7. The data points in these plots were collected after cropping the elevation maps to the largest possible continuous rectangular subsection. As a check of consistency, Allan variances collected along the $+x$ direction (from left-to-right) are plotted separately in Fig. 7 from those collected in the $+y$ direction (from top-to-bottom). The variograms demonstrate that nearly all of the lunar soil examples are well represented by fractal statistics over size domains from 0.1 mm to 1 cm. At scales larger than a few centimeters, the slope of the plots appears to change, most likely because we renormalized the elevation maps relative to a flat datum and because the size scale of measurements approaches the limiting size of the elevation maps. However, deviations from fractal behavior are not unusual

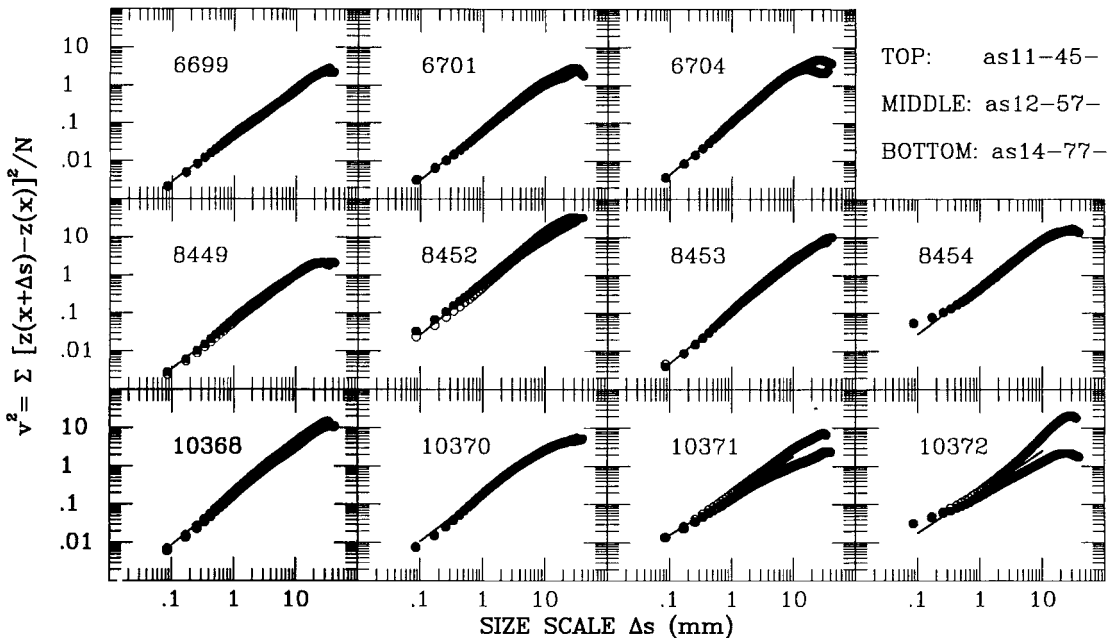


FIG. 7. Variogram plots for each of the 11 lunar maps. Solid dots represent Allan variances measured from left-to-right over the entire map. Open circles are Allan variances measured from top-to-bottom. Least-squares fit of a straight line (in log-log space) is shown only over the size scales (0.1 to 10 mm) for which the fits were performed. Fractal dimensions and rms slope angles of the surface at 1-mm scales obtained from the fits are reported in Table IV and Fig. 8.

in nature and generally indicate that different processes are operative at different physical scales (cf. Campbell and Shepard 1996, Shepard and Campbell 1998). *Apollo 14* examples 10371 and 10372 exhibit different behaviors in the $+x$ and $+y$ directions, perhaps indicating that some directional process (for example, slumping) has been operative in this area. These are both images of soil-covered rock for which the depth of soil cover significantly varies across the picture. *Apollo 12* example 8454, which represents unusually fluffy clods of regolith within a crater, also deviates from fractal behavior at very small scales (~ 1 mm).

We derived the fractal dimension and rms slope angle at 1-mm scale (Table IV) for each elevation map by performing least-squares fits of a simple power law to the variogram data in Fig. 7 over size scales from 0.1 mm to 1.0 cm. Figure 8 plots rms slope angle and fractal dimension D . Values of D range from 2.32 to 2.49. The rate of change of roughness with scale is remarkably similar for all regoliths ($\bar{D} = 2.36 \pm 0.03$) except soil-covered rock surfaces ($\bar{D} = 2.48 \pm 0.01$), which appear to become slightly smoother at size scales larger than typical Fra Mauro regolith. This latter behavior is because the *large-scale* roughness is dominated by the underlying rock and not by underlying regolith.

While the rate of change of roughness with spatial scale (D) is similar for most regoliths, the amplitude of roughness (Θ_{RMS})

TABLE IV
Fractal Analysis of ALSCC Elevation Maps

Picture number	Fractal	
	D	Θ_{RMS}
AS11-45-6699	2.40 ± 0.02	$12.1 \pm 0.3^\circ$
AS11-45-6701	2.35 ± 0.02	$14.2 \pm 0.1^\circ$
AS11-45-6704	2.32 ± 0.04	$18.0 \pm 0.1^\circ$
AS12-57-8449	2.38 ± 0.02	$13.9 \pm 0.6^\circ$
AS12-57-8452	2.34 ± 0.01	$37.0 \pm 1.5^\circ$
AS12-57-8453	2.32 ± 0.01	$18.3 \pm 0.3^\circ$
AS12-57-8454	2.38 ± 0.02	$34.5 \pm 1.3^\circ$
AS14-77-10368	2.34 ± 0.01	$23.2 \pm 0.8^\circ$
AS14-77-10370	2.39 ± 0.01	$23.0 \pm 0.1^\circ$
AS14-77-10371	2.49 ± 0.07	$22.2 \pm 1.6^\circ$
AS14-77-10372	2.47 ± 0.09	$24.6 \pm 2.3^\circ$

significantly varies among the regolith surfaces. Not unexpectedly, the rms slope variations strongly correlate with the widths of elevation histograms (σ) discussed earlier. Fluffy regolith clumps and soil surfaces with large stones exhibit fractal dimensions similar to typical undisturbed soils; however their amplitudes of roughness are significantly larger than those for mare or undisturbed Fra Mauro soils. Figure 8 suggests that mare

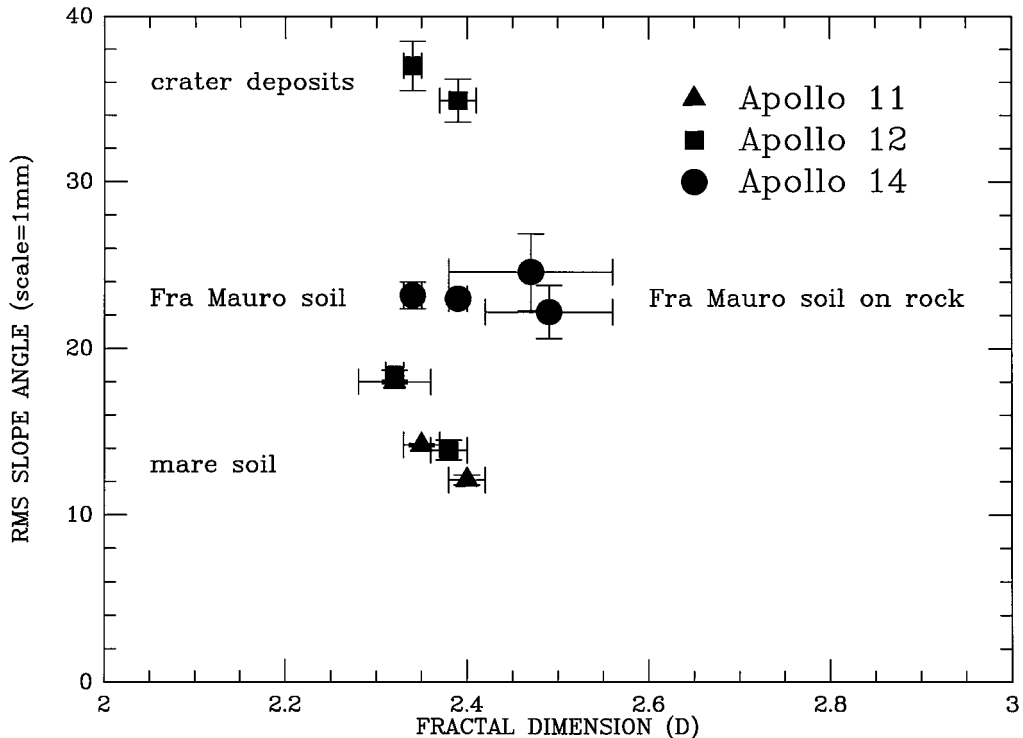


FIG. 8. Roughness amplitude (Θ_{RMS}) vs fractal dimension D derived from each digital elevation map. Nearly all soil types exhibit fractal dimensions near ~ 2.4 indicating that their rates of change of roughness with size scale are similar. Undisturbed mare and Fra Mauro soils are distinct by virtue of their contrasting roughness amplitudes (represented by the rms slope at 1-mm scale). Largest rms slope is for unusually fluffy clods of *Apollo 12* regolith inside a crater. The nearby *Apollo 12* point represents image AS12-57-8452 in which a significant part of the scene is covered by large, glazed stone within the crater.

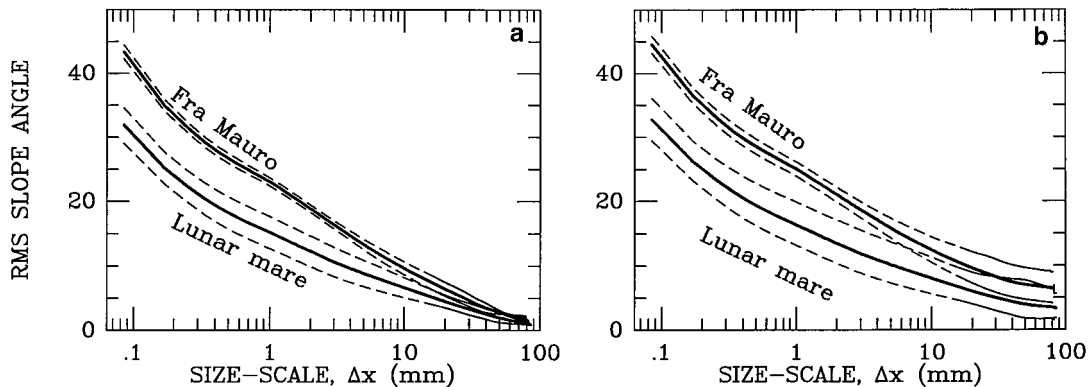


FIG. 9. (a) Average rms slope angles for undisturbed mare (*Apollo 11* and *12*) and Fra Mauro (*Apollo 14*) soils, respectively, measured as a function of size scale from digital topography maps after subtracting regional tilt. Solid lines are measured values and dashed lines represent one standard deviation about the mean. (b) Data from (a) after statistical restoration of the decimeter-scale roughness contribution (see text). Error envelopes (dashed lines) include the uncertainty in the large-scale roughness correction in addition to errors shown in (a).

and Fra Mauro soils can be distinguished from each other on the basis of rms slope. The mean amplitude of roughness for all Fra Mauro soils at 1-mm scale (mean $\Theta_{\text{RMS}} = 23 \pm 1^\circ$) is significantly larger than that for typical lunar mare soils (mean $\Theta_{\text{RMS}} = 15 \pm 3^\circ$).

The results in Table IV and Figure 8 provide a useful first-order comparison of the *relative* roughness of different regolith examples. However, before making a general comparison to remotely sensed data or to measurements from natural terrestrial surfaces, we must account for having subtracted out the regional tilt of the footprint area from each topographic map. Because we normalized elevations relative to a flat datum, we must now statistically restore an estimate of relief at size scales larger than the coverage of our maps (i.e., greater than ~ 1 dm). The problem is illustrated in Fig. 9a, which shows that the raw (tilt-subtracted) rms slopes angles for undisturbed Fra Mauro and Mare, respectively, appear to converge to zero at a size scale near 1 dm as a result of our initial normalization to a flat datum. Let $\tan \theta$ be the local topographic slope at a given small scale, Δx . To estimate the contribution of relief at decimeter and larger scales we must describe how the topographic map slope distribution, $a_s(\tan \theta, \Delta x)$, is perturbed by superposing or “painting” the subdecimeter-scale features on a larger surface that is smooth at subdecimeter scales but which itself has a nonzero distribution of decimeter and larger scale slopes. Let $a_l(\tan \theta)$ represent the distribution of slopes one would measure at decimeter scale if relief at subdecimeter scales were spatially unresolvable or if the surface were perfectly smooth at smaller scales. The addition of large-scale relief effectively broadens the slope distributions at smaller scales. The effective slope distribution for the combined small- and large-scale surfaces can be computed from the convolution of slope distributions

$$a_{\text{eff}}(\tan \theta, \Delta x) = \frac{\int_0^\infty a_s(\tan \theta - \tan \vartheta, \Delta x) a_l(\tan \vartheta) d(\tan \vartheta)}{\int_0^\infty a_l(\tan \vartheta) d(\tan \vartheta)}. \quad (7)$$

If the lunar surface was ideally smooth at decimeter and larger scale, $a_l(\tan \theta)$ would be unity at $\theta = 0$ and zero at all other slope angles. For this ideal case, Eq. (7) correctly predicts that $a_{\text{eff}}(\tan \theta, \Delta x) = a_s(\tan \theta, \Delta x)$.

To evaluate Eq. (7) and apply the correction to the data of Fig. 9a, we need to know the average large-scale slope distribution $a_l(\tan \theta)$ for mare and for Fra Mauro regoliths, respectively. We make the well-justified assumption that $a_l(\tan \theta)$ is Gaussian (Section 4.1) and constrain the widths of the distributions for Fra Mauro and typical mare, respectively, by requiring that their distribution means (rms slopes) match corresponding average regional tilt corrections from Table II. The rms average of tilt corrections obtained from undisturbed Fra Mauro regolith examples is $5.7^\circ \pm_{1.3}^{1.1}$, while that from undisturbed mare is $2.8^\circ \pm_{1.5}^{1.9}$. To evaluate $a_s(\tan \theta, \Delta x)$ we assume it is also Gaussian with a corresponding rms slope at Δx given by Fig. 9a. Figure 9b shows the rms slopes of Fra Mauro and mare regoliths, respectively, after the statistical restoration of large-scale roughness. The roughnesses at smallest scales are only slightly increased by the introduction of modest slopes at larger scale.

To test the realism of our approach, we consider analogous roughness reported in radar studies of the lunar surface. Unfortunately, we cannot directly compare radar rms slopes to our results because, as in the case of photometric measures of roughness, the relationship between the size scale of geological features and the radar wavelength used to detect them is poorly understood. At best, we can say that the size scale of geological features is likely at least as large as the radar wavelength, but perhaps as large as tens or hundreds of radar wavelengths. With this restriction in mind, we note that the curves of Fig. 9b flatten at decimeter scale and the rms slopes remain under 10° . Lunar radar rms slopes derived from centimeter-to-decimeter wavelengths are generally within this range as well (Simpson and Tyler 1982; Kroupenio *et al.* 1975; Kroupenio 1972, 1973; Tyler and Howard 1973; Hagfors 1970; Evans 1969; Muhleman *et al.* 1968a,b; Beckman and Klemperer 1965). Radar studies (cf. Simpson and Tyler 1982, Tyler and Howard 1973) also show that radar rms slope

angles of highland soils are typically about a factor of 2 to 3 larger than mare soils; similar to the factor of 2 obtained from our rms tilt corrections for Fra Mauro and mare, respectively. A more rigorous comparison between radar roughness studies and our topographic data can be made for the rate-of-change of roughness with scale (i.e., fractal dimension). An important consequence of the statistical restoration of large-scale roughness represented in Fig. 9b is that the *effective* fractal dimensions for mare and Fra Mauro must decrease relative to fractal dimensions that were determined prior to adding large-scale slopes. The curves in Fig. 9b imply an effective $D = 2.31 \pm 0.04$ for Fra Mauro and $D = 2.31 \pm 0.06$ for mare (evaluated as before over size scales from 0.1 mm to 1.0 cm). For comparison, Shepard *et al.* (1995) evaluated the fractal roughnesses implied from lunar radar studies and found $2.0 \leq D \leq 2.4$. Hagfors and Evans (1968) reported radar observations of the moon at wavelengths of 3.6, 68, and 600 cm, from which Shepard *et al.* estimate a fractal dimension $D \sim 2.2$ in reasonable agreement with our results. The corrected average $\Theta_{\text{RMS}} = 25^\circ \pm 1$ for Fra Mauro and $\Theta_{\text{RMS}} = 16^\circ \pm \frac{4^\circ}{3}$ for mare, respectively.

For the purposes of subsequent discussions, hereafter we adopt Fra Mauro regolith as a possible roughness analogue to typical highland regolith. This suggestion is supported by the fact that we find Fra Mauro rms slopes at large scale to be greater than those for mare by about the same amount as is implied for highlands relative to mare from radar studies (cf. Simpson and Tyler 1982, Tyler and Howard 1973). In addition, the rate of change of roughness with size scale (represented by fractal dimension D) for Fra Mauro regolith is typical of that for most lunar materials.

4.3. Photometric Roughness

A variety of radiative transfer models have been developed to describe the way rough particulate surfaces scatter light (for example, Hapke 1984, Lumme and Bowell 1981, Shkuratov *et al.* 1998). Hapke's (1984) photometric roughness model is widely applied in planetary surface photometry. Although the model was derived primarily as a correction to his smooth-surfaced photometric function (Hapke 1981), it has found increasing use as a remote-sensing tool to measure relative differences in subresolution-scale topographic roughness of geological surfaces. Hapke characterizes the macroscopic surface roughness using a single parameter; a mean topographic slope angle, $\bar{\theta}$, corresponding to an assumed Gaussian distribution of surface slopes. For average lunar mare and highland terrains, estimates of $\bar{\theta} = 8^\circ$ and 24° , respectively, have been derived from surface photometry (Helfenstein and Veverka 1987).

Hapke's photometric roughness parameter, $\bar{\theta}$, is difficult to interpret in a geological sense because it is not clear what size scale of geological features it represents—Hapke's model makes no assumption about the size scale of surface features that control photometric roughness other than that the roughness must occur at a scale that is smaller than the spatial resolution of the detector. Helfenstein (1988) investigated the contributions

of roughnesses at different size scales to measured values of $\bar{\theta}$ by using a synthetic (computer-generated) cratered surface representing scales from 1 m to 1 km and concluded that $\bar{\theta}$ is an integral measure of roughness in that it is affected by topography at all scales up to the size of the resolution of the detector. Shepard and Campbell (1998) more recently confirmed this finding with a generalized fractal model of surface roughness and demonstrated that, while photometric roughness was integral with decreasing size scale, for natural surfaces that obey fractal statistics, photometric roughness should be dominated by surface relief at the smallest scales for which the surface can be approximated by a distribution of topographic "facets." It is important to note that the studies of Helfenstein (1988) and Shepard and Campbell (1998) rely on artificial surfaces and computer modeling to investigate the contributions of topography at different size scales—as yet no one has tested values of $\bar{\theta}$ derived from photometry against *in situ* measurements of surface texture at size scales that are likely to be important in photometry.

Our present elevation map data set provides the first-ever means of investigating the geological significance of Hapke's roughness model using the true topographic roughness of a remotely sensed natural surface at size scales that critically affect photometric behavior. Below, we will use our elevation maps to explore the following questions: (1) How does $\bar{\theta}$ vary as a function of size scales on real regolith surfaces over the range from submillimeter to decimeter? (2) How do estimates of $\bar{\theta}$ obtained from lunar photometry compare with values derived directly from topographic data? (3) Can lunar mare and highland regoliths be distinguished from each other on the basis of photometric surface roughness? (4) Is Hapke's assumed Gaussian distribution of slopes valid for regolith surfaces? (5) Is Hapke's roughness parameter sensitive to departures from Gaussian behavior?

Hapke's formal definition of the $\bar{\theta}$ parameter derives from the weighted mean of topographic slopes

$$\tan \bar{\theta} = \frac{2}{\pi} \int_0^{\pi/2} a(\tan \theta) \sin \theta \tan \theta d\theta, \quad (8)$$

where θ is topographic slope angle and $a(\tan \theta)$ is the unidirectional distribution of slopes (i.e., the distribution of slopes as measured in a single direction from a topographic profile). Equation (8) can be numerically integrated to obtain $\bar{\theta}$ directly from a histogram of $a(\tan \theta) \sin \theta \tan \theta$ measured from unidirectional topographic profiles extracted from our elevation maps. This approach makes no a priori assumptions about the possible form of the slope distribution.

Hapke (1984) employed Eq. (8) by assuming that the unidirectional slope distribution is Gaussian with respect to slope (i.e., with respect to $\tan \theta$) defined such that the azimuth-independent slope distribution has the form

$$a(\tan \theta) \sin \theta d\theta = \frac{2}{\pi \tan^2(\bar{\theta})} \exp\left[-\frac{\tan^2 \theta}{\pi \tan^2 \bar{\theta}}\right] \sec^2 \theta \sin \theta d\theta. \quad (9)$$

Although Hapke assumes that the unidirectional slope distribution is Gaussian with a peak at $\tan \theta = 0$, the azimuth-independent distribution will generally be asymmetric with a nonzero peak because $a(\tan \theta)$ is weighted by $\sin \theta$ in Eq. (9). Since there could be a wide range of possible unidirectional slope distribution function which, when weighted by $\sin \theta$, yield similar azimuth-independent distributions, we expect that Hapke's Gaussian slope approximation may be satisfactory even if the true unidirectional slope distributions are not strictly Gaussian. Equation (9) provides a second method for determining $\bar{\theta}$ from topographic profiles at any chosen size scale: $\bar{\theta}$ can be determined by fitting the Gaussian distribution of Eq. (9) to measured histograms of $a(\tan \theta) \sin \theta$. However, Eq. (8) provides the preferred approach because the method of Eq. (9) is adversely sensitive to the coarse quantization of elevation increments that occurs in histograms at the smallest spatial scales (see below and Fig. 10).

We have used both of the above methods to measure $\bar{\theta}$ from our topographic maps over length scales from 0.085 to 85 mm (Table V). At each length scale, Δx , we collected histograms of $a(\tan \theta) \sin \theta$ and $a(\tan \theta) \sin \theta \tan \theta$ and binned them in uniform slope increments, $\Delta \tan \theta = \Delta z / \Delta x$, where Δz represents the nominal vertical resolution of our elevation maps (50 μm). Individual slopes were measured by fitting least-squares line

TABLE V
Photometric Roughness of Lunar Soils at Different Size-Scales

Picture	Photometric roughness ($\bar{\theta}$)			
	0.085 mm	0.85 mm	8.5 mm	85 mm
AS11-45-6699 ^b	37 ± 22°	11.4 ± 0.9°	4.3 ± 0.2°	1.4 ± 0.7°
AS11-45-6701 ^b	41 ± 25°	11.9 ± 0.8°	6.1 ± 0.1°	1.4 ± 0.5°
AS11-45-6704	44 ± 28°	14.0 ± 0.6°	7.7 ± 0.2°	1.2 ± 0.5°
AS12-57-8449 ^b	36 ± 21°	11.8 ± 1.0°	5.2 ± 0.2°	1.01 ± 0.2°
AS12-57-8452	47 ± 31°	16 ± 6°	17 ± $\frac{23}{17}$ °	3.0 ± 0.5°
AS12-57-8453 ^b	39 ± 22°	14.6 ± 0.7°	8.4 ± 0.5°	1.9 ± 0.3°
AS12-57-8454	46 ± 15°	21 ± 9°	13 ± 3°	2.0 ± 0.4°
AS14-77-10368 ^b	41 ± 23°	17 ± 3°	13 ± 2°	3 ± $\frac{11}{3}$ °
AS14-77-10370 ^b	42 ± 23°	17 ± 4°	8.3 ± 0.4°	1.5 ± 0.5°
AS14-77-10371	43 ± 21°	17 ± 3°	6.1 ± 0.1°	1.0 ± 0.5°
AS14-77-10372	45 ± 16°	17 ± 5°	8.2 ± 0.3°	1.3 ± 0.4°

^b Typical example of undisturbed lunar regolith.

segments to all points falling along a given traverse of baseline length Δx . Figure 10 compares examples of histograms of $a(\tan \theta) \sin \theta$ collected for three different orders of magnitude of length scales (0.1, 1.0, and 10 mm). As a result of our slope optimization criterion, bin widths decrease with

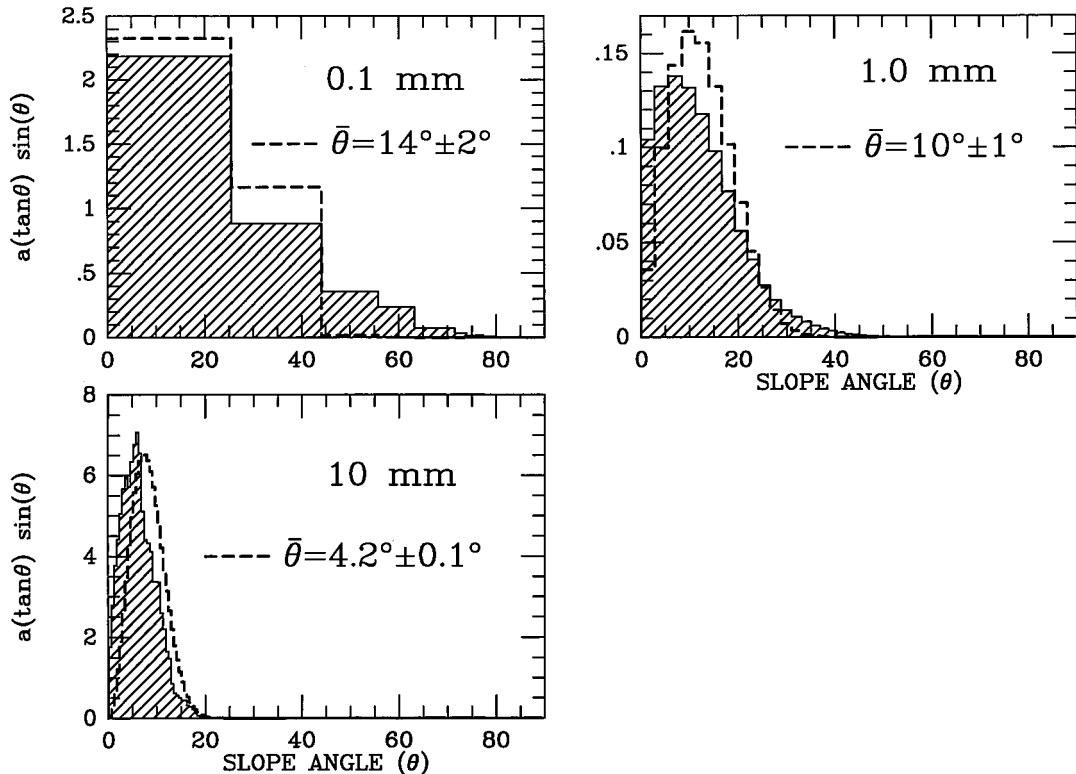


FIG. 10. Histograms of azimuth-independent slope distributions for AS11-45-6699 at three different size-scales (0.1, 1.0, and 10 mm). The data were binned in uniform increments of slope, although they are plotted here as a function of slope angle. The width of the bins vary with the size scale being measured, as described in the text. Dashed lines represent the best fit of an assumed Gaussian distribution of unidirectional slopes (see text for discussion). Also shown are the best-fit values of $\bar{\theta}$ from the Gaussian approximation (error bar is the difference in $\bar{\theta}$ between the best-fit Gaussian and direct integration of the histograms).

increasing size scale. To test the adequacy of Hapke's assumed Gaussian distribution of slopes, we used Eq. (9) to find values of $\bar{\theta}$ that best reproduce the slope histograms. At 0.1-mm scale, the histogram slope increments are large because the size scale is close to the vertical resolution of the elevation maps and the accuracy to which best-fit values of $\bar{\theta}$ can be found is somewhat poorer than at larger size scales for which slopes are binned in finer increments. As the size scale is increased, the histogram peaks become well defined and the Gaussian distribution appears to become a progressively better approximation to the actual slope distribution.

Table V lists values of $\bar{\theta}$ derived from direct evaluation of Eq. (8) for histograms obtained at four different size scales that range over four orders of magnitude from the resolution limit ($85 \mu\text{m}$) to the size limit of our maps ($\sim 85 \text{ mm}$). Error bars represent the magnitude of difference if $\bar{\theta}$ is estimated by fitting a Gaussian distribution of slopes to the histogram data (i.e., the method of Eq. (9)). Equation (9) consistently yielded smaller values of

$\bar{\theta}$ than the method Eq. (8). The results suggest that Hapke's Gaussian slope distribution function is a good approximation at scales larger than about 1 mm. At scales less than 1 mm, the Gaussian approximation appears to significantly underestimate $\bar{\theta}$; however, it is not clear how much of the inconsistency is due to the large bin sizes used in slope histograms at very small scales (see Fig. 10). In all cases, $\bar{\theta}$ decreases with increasing size scale (see also Fig. 11). At any given size scale, values of $\bar{\theta}$ for typical examples of lunar mare are similar to one another. Typical *Apollo 11* and *12* mare soils are not statistically distinguishable from one another on the basis of $\bar{\theta}$. However, values of $\bar{\theta}$ for *Apollo 14* Fra Mauro regoliths are generally larger than for mare soils. The relative variations in photometric roughness among terrains correlate well with similar variations in rms slope angle in Table IV.

In Fig. 11a we evaluated $\bar{\theta}$ over size scales from 0.1 mm to 8 cm and averaged results, respectively, for typical mare regoliths and for undisturbed Fra Mauro regoliths. However, as in

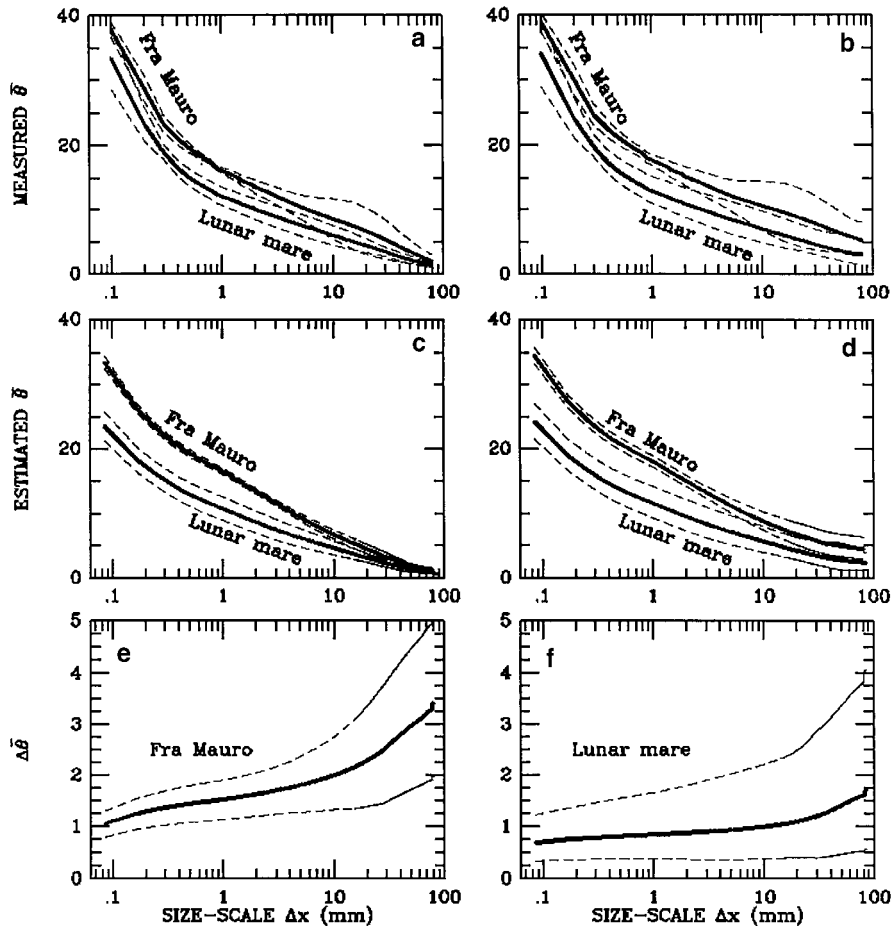


FIG. 11. (a) Average values of $\bar{\theta}$ for undisturbed mare (*Apollo 11* and *12*) and Fra Mauro (*Apollo 14*) soils, respectively, measured as a function of size scale from digital topography maps after subtracting regional tilt. Solid lines are measured values of $\bar{\theta}$ and dashed lines represent one standard deviation about the mean. (b) Data from (a) after statistical restoration of the decimeter-scale roughness contribution (see c–f). Error envelopes (dashed lines) include the uncertainty in the large-scale roughness correction in addition to errors shown in (a). (c) Model values of $\bar{\theta}$ obtained by applying Eq. (10) to the data of Fig. 9a. (d) Model values of $\bar{\theta}$ including statistical restoration of decimeter-scale roughness obtained by applying Eq. (10) to data of Fig. 9b. (e) $\bar{\theta}$ correction for decimeter-scale Fra Mauro roughness as a function of size scale obtained by subtracting the model Fra Mauro curve in (c) from the corresponding curve in (d). (f) Same as (e) but for lunar mare.

the case of our raw (tilt-subtracted) rms slope angle measurements (Fig. 9a), $\bar{\theta}$ converges toward zero at decimeter scales in Fig. 11a (and Table V) only because we have subtracted out the regional tilt of the footprint area to normalize elevations relative to a flat datum. To accurately compare terrain-average values of $\bar{\theta}$ to values reported from fits of Hapke's model to lunar photometry, we include a scale-dependent correction $\Delta\bar{\theta}$ (Figs. 11e, 11f) for the contribution of surface roughness at size scales larger than those represented in our elevation maps, as is done in Fig. 11b. As shown in Figs. 11c and 11d, we can derive $\Delta\bar{\theta}$ for mare and Fra Mauro regolith by first applying an approximate relationship between rms slope angle, Θ , and $\bar{\theta}$ (Shepard and Campbell 1998),

$$\tan(\bar{\theta}) = 0.7 \tan(\Theta), \quad (10)$$

to the data of Figs. 9a and 9b (as is done in Figs. 11a and 11b, respectively) and then by subtracting the curves in Fig. 11c from their counterparts in Fig. 11d (as is done in Figs. 11e and 11f). Although Eq. (10) is valid strictly for surfaces for $D = 2.5$ (in contrast to $D \sim 2.3$ that we have found for Fra Mauro and lunar mare surfaces), comparison of Figs. 11a and 11c demonstrates that Shepard and Campbell's (1998) approximation is excellent at nearly all size scales greater than about 0.2 mm and slightly underestimates $\bar{\theta}$ as smaller scales. The values of $\Delta\bar{\theta}$ are largest near the upper size limit of our elevation maps (~ 8 cm) and

least significant (about a degree or less) at the smallest scales (~ 0.1 mm). This is an important result because if photometrically detected roughness is most representative of large slopes which occur at the smallest size scales, then the accuracy to which we can measure the most important size scale is relatively insensitive to any uncertainties in our large-scale roughness correction. In Fig. 11b we have added $\Delta\bar{\theta}$ to the data, Fig. 11a, to obtain corrected curves of $\bar{\theta}$ vs size scale. Figure 11b shows that, especially at the smallest scales of our data, the photometric roughness of Fra Mauro regolith is measurably greater than that of lunar mare, but the difference is not very large at any single common scale.

Fits of Hapke's model to lunar photometric data (Helfenstein and Veverka 1987) imply that the photometric roughness of lunar highlands ($\bar{\theta} = 24^\circ$) should be three times larger than that for lunar mare ($\bar{\theta} = 8^\circ$). Numerical values of $\bar{\theta}$ for Fra Mauro regolith from Fig. 11b best match $\bar{\theta} = 24^\circ$ for average highlands terrains derived from lunar photometric observations (Helfenstein and Veverka 1987) at a size scale of 0.33 mm. In contrast, numerical values of $\bar{\theta}$ for lunar mare (Fig. 11b) best match $\bar{\theta} = 8^\circ$ from lunar photometry at a size scale of 6.5 mm—a factor of 20 larger than the size scale that appears representative of highland regolith. There is no obvious reason to expect that the size scale representative of $\bar{\theta}$ for mare should be significantly larger than that for highland regolith. Figure 12 shows that there is no single size scale for which $\bar{\theta}$ measured for Fra Mauro regolith from

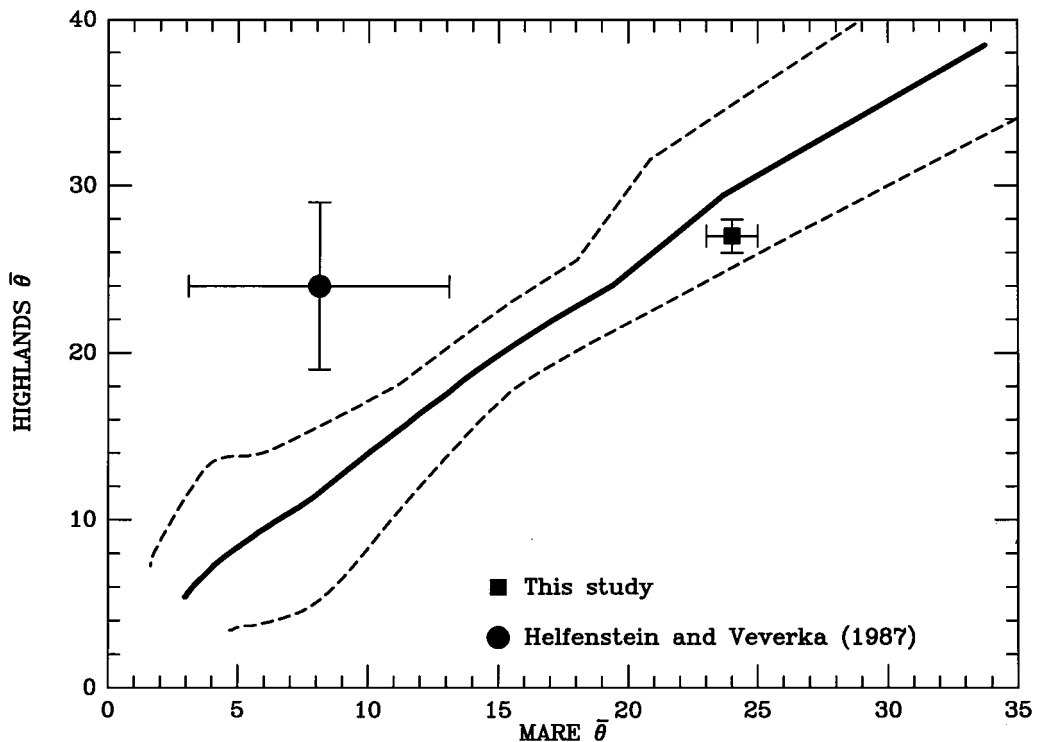


FIG. 12. Comparison of Fig. 11b values of $\bar{\theta}$ for highland (Fra Mauro) regolith to those for mare at each spatial scale. Dashed lines envelope the range of uncertainties in average values of $\bar{\theta}$ from Fig. 11b. The data point from Helfenstein and Veverka (1987) is derived from lunar photometry and falls well outside of the uncertainty envelope. New fits photometric estimates of $\bar{\theta}$ derived in this study (Fig. 13) better agree with topographic estimates at a common size scale.

our topographic maps is larger than that for mare by the factor of 3 implied by the photometric estimate from Helfenstein and Veverka (1987). We resolve these inconsistencies in Section 5.1.

In summary, we have found that the photometric roughness of highland regolith is generally larger than that of mare soils, but not by as large a margin than is implied from early photometric modeling. There appears to be no single size scale for which $\bar{\theta}$ measured from our topographic maps simultaneously match mare and highland values reported from lunar photometry in Helfenstein and Veverka (1987). For typical lunar regolith surfaces, the relative contribution to $\bar{\theta}$ from surface relief at scales of 8 cm and larger is small in comparison to the contribution from surface relief at submillimeter scales.

5. DISCUSSION

5.1. Photometric Roughness

In Section 4.3 we found that the photometric roughness of undisturbed Fra Mauro regolith is larger than that of undisturbed mare soils at all size scales (though not by a large margin). We also found that there is no single size scale for which $\bar{\theta}$ measured from our topographic maps simultaneously match photometrically derived mare and highland values from Helfenstein and Veverka (1987). The size scale at which Helfenstein and Veverka's $\bar{\theta} = 8^\circ$ for mare was best matched is a factor of 20 larger than the best match $\bar{\theta} = 24^\circ$ for highland soils. In addition, there is no single size scale for which highland soils are three times rougher than mare soils as implied from lunar photometry.

It is not clear why the size scales that best match photometric estimates of $\bar{\theta}$ for mare and highland surfaces should differ by a factor of 20. There are several possible explanations for the inconsistency that we can consider here. First, it is possible that the limited suite of examples we have examined in this study is not truly representative of average highland and mare soils. However, the *Apollo* astronauts chose the photographic sites at random, and we expect that our examples are representative because we find no statistically significant differences in $\bar{\theta}$ among typical *Apollo 11* and *12* mare soils. Second, it is possible that we have not adequately accounted for the contributions of roughness at all scales greater than 8 cm in Fig. 11b. However, as Figs. 11e and 11f show, the contribution to $\bar{\theta}$ from relief at decimeter and larger scales have only a small effect on the relatively large roughness at very small scales (~ 0.1 mm) that are expected to have the strongest effects on photometric behavior (Hapke 1984, Helfenstein 1988, Shepard and Campbell 1998). Third, it is possible that the size scale of roughness that $\bar{\theta}$ represents truly *does* vary among terrains. Shkuratov and Stankevich (1997) and Shepard and Campbell (1998) have proposed that the smallest representative size scales for $\bar{\theta}$ may be different for soil surfaces composed of constituent particles exhibiting contrasting optical properties. For example, for surfaces composed of high-albedo particles, roughness at very small scales may be photometrically undetectable because multiple scattering of light between particles and interstitial voids in the regolith attenuate projected shadows (Buratti and Veverka 1985). However,

the behavior we see is opposite—smaller scales appear to be detectable on the highland surface which is higher in albedo than lunar mare.

Perhaps the most likley explanation is that the Hapke photometric model used in Helfenstein and Veverka (1987) was too simplistic to accurately retrieve the absolute roughnesses of different lunar terrains. In the past decade, a variety of developments in photometric theory have lead to improvements in Hapke's model. Among the most significant improvements are the incorporation of realistic particle phase functions (Bowell *et al.* 1989; Clark *et al.* 1999; Domingue *et al.* 1991, 1995; Domingue and Hapke 1992; Domingue and Verbiscer 1997; Helfenstein *et al.* 1991, 1997, 1999; Simonelli *et al.* 1998; Thomas *et al.* 1996; Verbiscer and Helfenstein 1998; Hartman and Domingue 1998) and the discovery that coherent backscatter and shadow-hiding mechanism both contribute to the opposition effects of planetary surfaces (Buratti *et al.* 1996; Hapke *et al.* 1993, 1998; Helfenstein *et al.* 1997, 1999; Hillier *et al.* 1999; Mishchenko 1992; Mishchenko and Dlugach 1992, 1993; Shkuratov 1988; Shkuratov and Ovcharenko 1998; Shkuratov *et al.* 1999). Helfenstein *et al.* (1997) altered Hapke's (1981, 1984, 1986) equation to include a realistic particle phase function (Kattawar 1975) and simultaneous modeling of shadow-hiding (Hapke 1986) and coherent-backscatter (Mishchenko 1992) opposition effects, and then tested it on whole-disk and disk-resolved photometry of the lunar surface. Among their findings was that the more sophisticated Hapke model results in a significantly larger average lunar value of $\bar{\theta} = 26.7 \pm 0.1^\circ$ than the corresponding estimate of $\bar{\theta} = 20.0 \pm 0.6^\circ$ from Helfenstein and Veverka (1987).

To see if the Hapke/Mishchenko model used by Helfenstein *et al.* (1997) leads to significantly different photometric estimates of $\bar{\theta}$ for mare and highlands, we fit it to the same disk-resolved data set (Shorthill *et al.* 1969) for dark (mare), average, and bright (highland) terrains used in Helfenstein and Veverka (1987). These data cover phase angles $2.3^\circ \leq \alpha \leq 135.7^\circ$, incidence angles $1.9^\circ \leq i \leq 89.6^\circ$, and emission angles $4.0^\circ \leq e \leq 135.7^\circ$. The available range of phase angles is inadequate to simultaneously constrain the coherent-backscatter and shadow-hiding opposition surge parameters, and coverage does not extend to large enough phase angles to fully constrain the three model parameters for the particle phase function. However, because $\bar{\theta}$ can be constrained by limb-darkening behavior, reasonable estimates of $\bar{\theta}$ do not demand the data at all available phase angles: We can obtain acceptable estimates by restricting the fit to phase angles where the contribution from the opposition effect is small ($\alpha \geq 30^\circ$) and the forward-scattering contribution from the particle phase function is not large ($\alpha < 135^\circ$). Following Helfenstein *et al.* (1997), we also restricted $i \leq 75^\circ$ and $e \leq 80^\circ$. Using the grid-search approach of Helfenstein *et al.* (1997), we sought values for only two model parameters, $\bar{\theta}$ and ω_0 (the average particle single-scattering albedo), that minimize the rms residuals between the photometric data and model predictions. The remaining six model parameters were fixed at the values derived by Helfenstein *et al.* (1997).

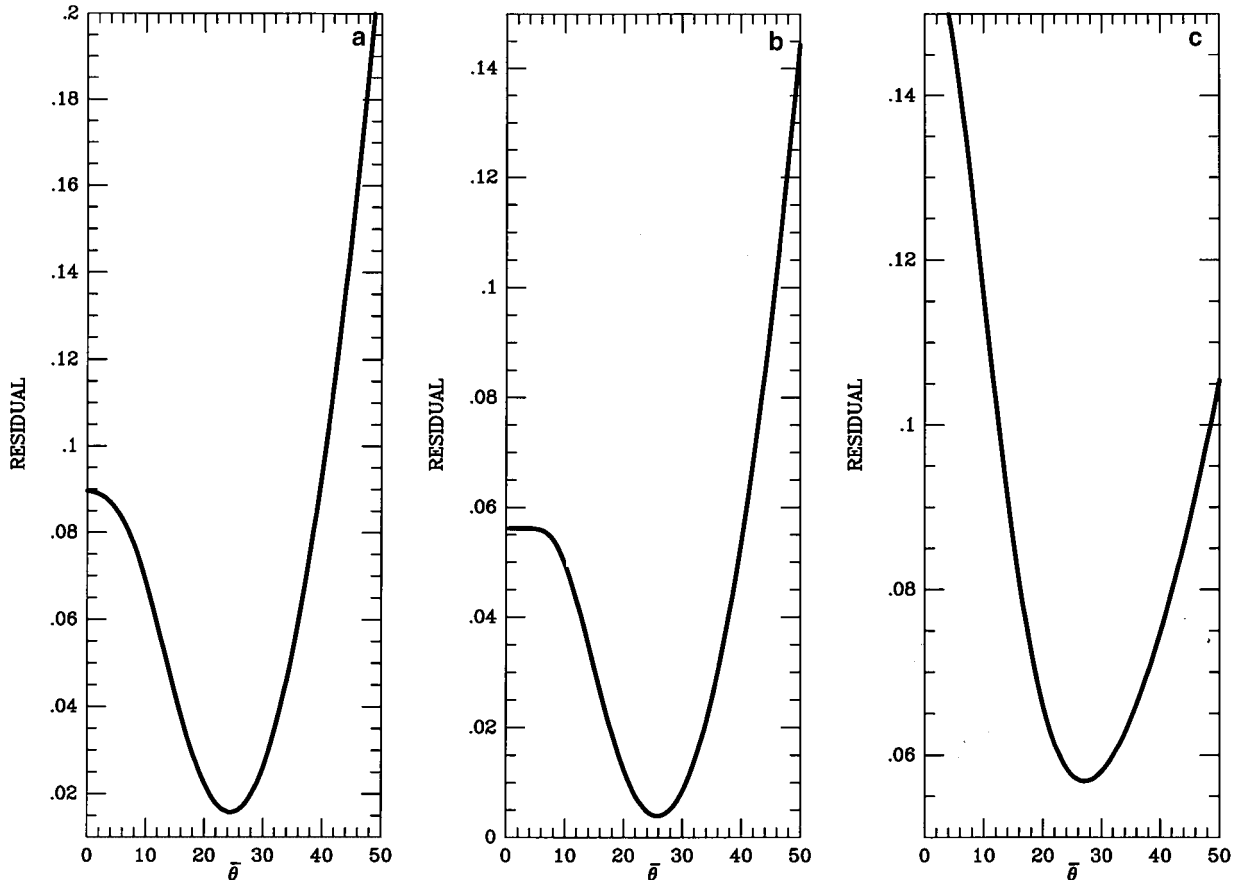


FIG. 13. Results of parameter grid search to find least-squares fit values of $\bar{\theta}$ for three lunar terrains previously examined by Helfenstein and Veverka (1987). A distinct minimum in the curves identifies the solution value. (a) Solution for mare (dark terrain of Shorthill *et al.* 1969) gives $\bar{\theta} = 24 \pm 1$ and $\omega_0 = 0.16 \pm 0.03$. (b) Solution for average lunar terrains gives $\bar{\theta} = 26 \pm 1$ and $\omega_0 = 0.31 \pm 0.03$, and (c) solution for highlands (bright terrain of Shorthill *et al.* 1969) gives $\bar{\theta} = 27 \pm 1$ and $\omega_0 = 0.40 \pm 0.03$.

The results of the grid-searches are shown in Fig. 13, where we plot rms residuals as a function of assumed $\bar{\theta}$. We obtained $\bar{\theta} = 27 \pm 1^\circ$ for bright (highlands), $\bar{\theta} = 26 \pm 1^\circ$ for average, and $\bar{\theta} = 24 \pm 1^\circ$ for dark (mare). The value of $\bar{\theta} = 26 \pm 1^\circ$ for average terrain is not statistically different from the global average value of $\bar{\theta} = 26.7 \pm 1^\circ$ derived in Helfenstein *et al.* (1997) and indicates that we have retained enough photometric coverage to adequately constrain $\bar{\theta}$ in all three cases. As in Helfenstein and Veverka (1987), the value of $\bar{\theta}$ for average lunar materials falls sensibly in between those for smoother mare and rougher highland materials. Figure 12 suggests that the new photometric values for highlands and mare, respectively, both represent similar size scales in our topographic measurements. Specifically, our new photometric estimate of $\bar{\theta} = 27 \pm 1^\circ$ for highlands best matches Fig. 11b at a size scale of $0.26 \pm_{0.06}^{0.05}$ mm, and our new photometric estimate of $\bar{\theta} = 24 \pm 1^\circ$ for mare is best matched in Fig. 11f at size scales of $0.20 \pm_{0.05}^{0.07}$ mm. Within the expected uncertainty, these two size scales are not statistically distinguishable from each other (see also Fig. 12). We conclude that, for typical lunar soils, $\bar{\theta}$ is representative of the cumulative contribution of surface relief at all size scales larger than about 0.1 mm.

The fact that our estimates of $\bar{\theta}$ from lunar photometry correspond to very small size scales is consistent with the expectation that the largest average topographic slopes occur at dimensions where interparticle cohesive forces can overcome gravity (Hapke 1984, Helfenstein 1988, Shepard and Campbell 1998). Figure 11f (see also Table V) suggests, however, that at scales of 0.1mm and smaller, values of θ exist which are significantly larger than those found from fits to lunar photometry data. The implication is that there is a size scale below which topographic relief either is not photometrically detectable or is not represented in the Hapke model as “macroscopic” roughness. The former possibility has recently been considered by Shepard and Campbell (1998) who proposed that large roughnesses at very small scales may be photometrically undetectable because multiple scattering of light between particles and interstitial voids in the regolith attenuate projected shadows (see also Buratti and Veverka (1985) and Shkuratov and Stankevich (1997)). This hypothesis predicts that the size scale that $\bar{\theta}$ represents depends on the albedo of the surface—high albedos with significant multiply scattered light restrict $\bar{\theta}$ to larger size scales than for low-albedo surfaces where multiple scattering is weak. The slightly larger numerical value for the size scale of photometric

roughness for highland regolith ($0.26 \pm \frac{0.05}{0.06}$ mm) than for mare ($0.20 \pm \frac{0.07}{0.05}$ mm) is consistent with Shepard and Campbell's hypothesis; however, as noted earlier the difference may not be statistically significant.

The alternative (or perhaps complementary) hypothesis, that topographic relief at size scales smaller than 0.2 mm is not represented as macroscopic roughness, requires that the photometric effects of this very small scale roughness be described by some other component of the Hapke model. The most logical possibility is that topographic relief at such small scales falls into the same physical realm and is modeled as the shadow-hiding opposition surge (Hapke 1986). This possibility is especially relevant to the geological interpretation of Hapke model parameters. Hapke's (1984) macroscopic roughness model assumes that the optical interactions are taking place on a faceted surface. Hapke's (1986) shadow-hiding opposition effect model assumes that the optical interactions are taking place among a loose aggregate of individual particles in mutual contact. In the context of this hypothesis, our results would suggest that we have found the threshold below which optical interactions are better represented as occurring among a loose particle aggregate than a light scattered from a faceted surface (see also Shepard and Campbell (1998)).

While it is beyond the scope of the current paper to do so, both of the above hypotheses may be tested with our digital elevation maps of lunar regolith. By applying computer ray-tracing techniques to the digital maps at a variety of different assumed illumination and viewing geometries, it should be possible to model the extent to which multiply scattered light attenuates shadows projected by topographic features at different size scales. Following the method of Helfenstein (1988), it should also be possible to simulate reflectance phase curves from the elevation maps to compare with actual lunar photometric phase curves and determine if topographic relief at size scales greater than $0.085 \mu\text{m}$ significantly contributes to the shadow-hiding opposition effect.

Our immediate conclusions have a variety of important implications for photometry of planetary surfaces and laboratory goniophotometric studies. In nearly all applications of Hapke's model to planetary photometry, it is generally assumed that the photometric roughness estimated from whole-disk photometry represents the same physical quantity as when $\bar{\theta}$ is derived from disk-resolved measurements¹ even though whole-disk observations include an additional contribution of surface relief covering size scales extending several orders of magnitude larger than the spatial resolution of typical disk-resolved data. By demonstrating that topographic relief at scales larger than decimeter scales do not typically contribute much to the observed photometric roughness we have shown that this assumption is valid. Laboratory spectrogoniometric measurements of particulate samples are usually obtained from sample dishes that are millimeters to centimeters in size. When applying Hapke's photometric

model to analyze such laboratory measurements, it is often assumed that the samples are macroscopically smooth (i.e., it is assumed that $\bar{\theta} = 0^\circ$). Our results show that the most important contributions to $\bar{\theta}$ come from surface relief at submillimeter size scales—smaller than typical dimensions of laboratory sample dishes. Consequently, in the analysis of spectrogoniometric data from laboratory specimens, it may be important to consider the effects of photometric roughness, especially in observations obtained at relatively large incidence, emission, or phase angles.

5.2. Geological Implications

Among our most significant findings is that three different measures of roughness (rms slope angles, elevation histograms, and Hapke's photometric roughness parameter) indicate that undisturbed Fra Mauro regolith is rougher than lunar mare at all size scales greater about 0.1 mm. The same measures of roughness reveal no significant difference in the average textural characteristics of soils from two different mare sites (*Apollo 11* Mare Tranquilitatis and *Apollo 12* Oceanus Procellarum).

At approximately centimeter and larger size scales, the comparable roughnesses of *Apollo 11* and *12* regoliths and the larger *Apollo 14* regolith roughness are easily explained. *Apollo 11* and *12* lunar mare were emplaced as relatively smooth, inviscid-lava flows, whereas Fra Mauro originated as a massive ejecta deposit from the Imbrium basin and was probably quite hummocky and rough. While differences in the way Fra Mauro and lunar mare were emplaced may also explain the persistence down to submillimeter scales of the roughness dichotomy between mare surfaces and Imbrium basin ejecta, further consideration is warranted. Because the *Apollo 11* and many of the *Apollo 12* ALSCC pictures were obtained in close proximity to the lunar module, it is possible that they show soil surfaces that have been scoured by the descent engine's rocket blast. *Apollo 14* ALSCC images were acquired far enough away from the lunar module that scouring from the rocket blast is not a concern. The relative consistency in our roughness estimates from different examples of "undisturbed mare soils" at different sites suggest that rocket blast erosion did not significantly affect the targets in the ALSCC images that we selected for study. Rms slope angles at 1-mm scale from Table IV imply that Imbrium basin ejecta and mare regolith roughnesses continue to differ, even after subtracting the decimeter-scale slopes. Table V (see also Fig. 11) suggests, however, that the difference becomes increasingly less significant with decreasing size scale below 1 cm. At these small (subcentimeter) scales, the size distribution and cohesiveness of regolith grains could play a significant role in controlling surface texture so that it is worth examining the extent to which grain sizes differ among lunar soil samples collected nearby the ALSCC locations.

The size distribution of particles in lunar regolith is strongly related to regolith maturity. Mature soil has a smaller mean grain size than immature soil because it has had a longer exposure to the comminuting effects of micrometeorite impacts. An immature soil can evolve to maturity on time scales of several hundred million years if not influenced by addition of immature material

¹ It is also often assumed that the whole-disk observations are dominated by terrain of a single type.

TABLE VI
Maturity of Soil Samples Obtained Near ALSCC Locations

Site	Picture	Soil sample	Maturity ^a		
			I_s/FeO	Classification	
<i>Apollo 11</i>	AS11-45-6699	10010	75.0	Mature	
	Mare	AS11-45-6701	10011	69.0	Mature
	Tranquilitatis	AS11-47-6704	10084	78.0	Mature
<i>Apollo 12</i>	AS12-57-8449	12001	56.0	Submature	
	Oceanus	AS12-57-8452	12003	57.0	Submature
	Procellarum		12070	47.0	Submature
<i>Apollo 14</i>	AS14-77-1068	14259	85.0	Mature	
	Fra Mauro	AS14-77-1070			

^a From Morris (1978).

from subsequent impacts (cf. McKay *et al.* 1991 and references therein). A widely used index of regolith maturity is I_s/FeO , where I_s is the measured ferromagnetic resonance intensity and FeO represents the total Fe content of the sample (Morris 1978). Three maturity levels are typically defined (McKay *et al.* 1974): immature soils with $0.0 \leq I_s/\text{FeO} \leq 29.0$ units, submature soils with $30.0 \leq I_s/\text{FeO} \leq 59.0$ units, and mature soils with $I_s/\text{FeO} \geq 60.0$ units. Table VI identifies soil samples that were collected nearest the ALSCC sites and their corresponding maturities. The similarity in submillimeter-to-subcentimeter scale roughnesses of *Apollo 11* and *12* soils and their mutual difference from *Apollo 14* examples is evidently not a strong function of lunar regolith grain-size variations. On the basis of Table VI, one would expect that *Apollo 11* (mature) and *Apollo 12* (submature) surfaces should be texturally different and that *Apollo 11* and *14* (mature) surfaces would be texturally similar. This is not the case and we may conclude that the submillimeter-scale roughness of the lunar terrains is not a sensitive measure of regolith maturity.

Another significant result of our study is that lunar surface roughness at submillimeter-to-subcentimeter scales is well represented by fractal statistics (i.e., a simple power law is sufficient to relate the decrease in average slopes with increasing length scales). In contrast to results of radar studies that reveal significant differences in fractal dimension with terrain type, however, our study shows that overall the fractal dimensions of a variety of lunar soils are remarkably similar at size scales smaller than those important in radar studies. One interpretation of this result is that, at subcentimeter scales, *the rate that roughness increases with decreasing size scale* is largely controlled by regolith gardening processes that evolve the top centimeter of regolith on relatively short times scales. Note that we found a larger fractal dimension for soil-covered rock surfaces ($D = 2.41 \pm_{0.07}^{0.12}$)² than for regolithic surfaces ($D = 2.31 \pm 0.06$). The larger value

of D for the soil-covered rock surfaces is mostly due to the relative absence of subdecimeter-scale topographic undulations on the gently sloping rock from which the ALSCC images were obtained. This is qualitatively clear from Fig. 5 elevation profiles, which show that the soil-covered rock surfaces and typical lunar mare surfaces have very similar visual textures at very small scales (i.e., near the limit of the map resolution). The value of $D = 2.41$ for soil-covered rock is similar to values derived from studies of centimeter and larger scale roughnesses of terrestrial basalt flows (Farr 1992; Campbell and Shepard 1996; Shepard and Campbell 1995, 1998). Farr (1992) studied differences in the fractal dimensions Cima Volcanic flows (Mojave desert) of different ages and erosional states. Farr found $D = 2.49$ for the freshest flow (16000 years), but values for older, more highly weathered flows often exhibited smaller values $2.27 \leq D \leq 2.46$.

6. CONCLUSIONS

Using digital elevation maps derived from stereophotogrammetry of Apollo lunar surface closeup camera images, we have demonstrated that average undisturbed Fra Mauro regolith is rougher than lunar mare regolith over all size scales from 0.085 to 85 mm. We confirm the earlier result of Lumme *et al.* (1985) that cumulative distributions of regolith elevation are well represented by Gaussian statistics. At the same time, we show that cumulative distributions are relatively insensitive to asymmetries in the detailed shapes of elevation histograms and that significant deviations from Gaussian behavior is demonstrated in about half of the elevation histograms we studied. We also confirmed Lumme *et al.*'s finding that the roughnesses of most lunar regolith surfaces increase with decreasing size scale. In addition, we find that this behavior is well represented by fractal statistics. The rates of change of roughness with size scale, represented by fractal dimension D , are remarkably similar among average terrains. After correcting for the contribution of large-scale roughness, our average value of $D = 2.31 \pm 0.06$ falls within the range $2.0 \leq D \leq 2.4$ reported from lunar radar studies (Shepard *et al.* 1995). We find a larger value ($D = 2.41 \pm_{0.07}^{0.12}$) for a gently sloping soil-covered rocky surface. The amplitude of roughness, which we characterize with the rms slope angle at 1-mm scale, varies significantly among terrains. For lunar mare, the average rms slope angle at 1-mm scale is $16 \pm 3^\circ$ while that for undisturbed Fra Mauro regolith is $25 \pm 1^\circ$. Comparison of our results radar roughness data shows that Fra Mauro regolith (Imbrium basin ejecta) exhibits similar roughness to lunar highland surfaces. While undisturbed Fra Mauro regolith surfaces are rougher than mare surfaces at all scales, the contrast in roughness between the two regolith types is less significant at subcentimeter scales than it is at larger scales.

We have verified both from direct measurement of topography and from fits to disk-resolved lunar photometric observations that the photometric roughness of lunar highland regolith is larger than mare regolith. Values of Hapke's photometric roughness parameter ($\bar{\theta}$) derived from lunar photometry (Helfenstein

² The method of Section 4.3 has been used to adjust for the contribution of large-scale roughness. An average tilt correction of $2.7 \pm 0.5^\circ$ (Table II) was adopted and a new fractal $D = 2.41 \pm_{0.07}^{0.12}$ and $\Theta_{\text{RMS}} = 24 \pm 2^\circ$ were determined from the corrected data.

and Veverka 1987) are found to be quantitatively inaccurate, probably due to the simplicity of the early Hapke photometric model that was used in that study. Fits of a more recent Hapke model, that includes a description of realistic particle phase functions and the coherent backscatter opposition effect, yield estimates of $\bar{\theta} = 27 \pm 1^\circ$ for highlands and $\bar{\theta} = 24 \pm 1^\circ$ for mare. These values of $\bar{\theta}$ as well as the implied relative highland : mare photometric roughness ratio are best matched from our elevation data by the cumulative contributions of surface topography covering all scales greater than 0.1 mm. Less than 5% of the photometrically detected roughness of lunar regolith is contributed by surface relief at scales larger than 8 cm. This conclusion implies that values of $\bar{\theta}$ derived from whole-disk and disk-resolved photometry, respectively, may be taken to represent the same physical quantity. In addition, particulate samples used in goniophotometric measurements should not be assumed to be photometrically smooth (i.e., $\bar{\theta} = 0^\circ$), as is often done in laboratory applications of Hapke's photometric model. The predicted photometric roughness at size scales of about 0.1 mm and less significantly exceed photometric estimates. This result suggests that there exists a size scale below which topographic relief either is not photometrically detectable or is not represented in the Hapke model as "macroscopic" roughness.

ACKNOWLEDGMENTS

This study was supported by NASA Grants NAG5-3639, NAG5-4000, and NAGW-4986. We are grateful to T. Gold for providing Apollo Closeup Stereo Pictures, R. Kline for access to Apollo Hasselblad pictures, S. Singer (SRS Unlimited) for photographic processing, B. Campbell (National Air and Space Museum) for providing computer space for digital data transfers, and M. Roth for help with manuscript preparation. We thank B. Buratti and R. Korotev for constructive reviews and J. Veverka, N. Solomon, and W. Botke for helpful suggestions.

REFERENCES

- Allan, D. W. 1966. Statistics of atomic frequency standards. *Proc. IEEE* **54**, 221–230.
- Anderson, A. T. 1971. Apollo 14 Photography, Part II, 70-mm, 35-mm, 16-mm, and 5-in Frame Index. National Space Science Data Center, NASA GSFC, Greenbelt, MD.
- Anderson, A. T., and M. A. Niksch 1971. Apollo 14 Lunar Photography, Part I, Data Users' Note (NSSDC 71-008A-01). National Space Science Data Center, NASA GSFC, Greenbelt, MD.
- Bean, A. L., C. Conrad, Jr., and R. F. Gordon 1970. Crew observations. In *Apollo 12 Preliminary Science Report*, NASA SP-235, pp. 29–38.
- Beckmann, P., and W. K. Klemperer 1965. Interpretation of the angular dependence of backscattering from the Moon. *J. Res. Natl. Bur. Stan.* **69D**, 1669–1677.
- Bowell, E., B. Hapke, D. Domingue, K. Lumme, J. Peltoniemi, and A. W. Harris 1989. Applications of photometric models to asteroids. In *Asteroids II* (R. Binzel, T. Gehrels, and M. Matthews, Eds.), pp. 524–556. Univ. of Arizona Press, Tucson.
- Buratti, B. J. 1991. Ganymede and Callisto: Surface textural dichotomies and photometric analysis. *Icarus* **92**, 312–323.
- Buratti, B. 1995. Photometry and surface structure of the icy Galilean satellites. *J. Geophys. Res.* **100**, 19,061–19,066.
- Buratti, B., and J. Veverka 1985. Photometry of rough planetary surfaces: The role of multiple scattering. *Icarus* **64**, 320–328.
- Buratti, B., J. Hillier, and M. Wang 1996. Lunar opposition surge: Observations by Clementine. *Icarus* **124**, 490–499.
- Campbell, B., and M. K. Shepard 1996. Lava flow surface roughness and depolarized radar scattering. *J. Geophys. Res.* **101**, 18,941–18,951.
- Chase, C. G. 1992. Fluvial land sculpting and the fractal dimension of topography. *Geomorphology* **5**, 39–57.
- Chou, Y. 1972. *Probability and Statistics for Decision Making*. Holt, Rinehard and Winston, New York.
- Clark B. E., J. Veverka, P. Helfenstein, P. C. Thomas, J. F. Bell, III, A. Harch, M. S. Robinson, S. L. Murchie, L. McFadden, and C. Chapman 1999. NEAR photometry of Asteroid 253 Mathilde. *Icarus* **140**, 53–65.
- Davis, J. R., and D. C. Rohlfs 1964. Lunar radio-reflection properties at decimeter wavelengths. *J. Geophys. Res.* **69**, 3257–3262.
- Domingue, D., and B. W. Hapke 1992. Disk-resolved photometric analysis of european terrains. *Icarus* **99**, 70–81.
- Domingue, D., and A. Verbiscer 1997. Re-analysis of the solar phase curves of the icy Galilean satellites. *Icarus* **128**, 49–74.
- Domingue, D., B. W. Hapke, G. W. Lockwood, and D. T. Thompson 1991. Europa's phase curve: Implications for surface structure. *Icarus* **90**, 30–42.
- Domingue, D., D. L. Lockwood, and D. T. Thompson 1995. Surface textural properties of icy satellites: A comparison between Europa and Rhea. *Icarus* **115**, 228–249.
- Evans, J. V. 1969. Radar studies of planetary surfaces. *Annu. Rev. Astron. Astrophys.* **7**, 201–248.
- Farr, T. 1992. Microtopographic evolution of lava flows at Cima Volcanic Field, Mojave Desert, California. *J. Geophys. Res.* **97**, 15,171–15,179.
- Gold, T. 1969. Lunar surface closeup stereoscopic photography. In *Apollo 11—Preliminary Science Report*, NASA SP-214, pp. 187–197. NASA, Washington, DC.
- Gold, T. 1970. Apollo 11 and 12 close-up photography. *Icarus* **12**, 360–375.
- Gold, T. 1971. Lunar-surface closeup stereoscopic photography. In *Apollo 14—Preliminary Science Report*, NASA SP-272, pp. 239–247. NASA, Washington, DC.
- Gold, T., F. Pearlce, and R. Jones 1970. *Apollo 12—Preliminary Science Report*, NASA SP-235. NASA, Washington, DC.
- Hagfors, T. 1968. Relations between rough surfaces and their scattering properties as applied to radar astronomy. In *Radar Astronomy* (J. Evans and T. Hagfors, Eds.), pp. 187–218. McGraw-Hill, New York.
- Hagfors, T. 1970. Remote probing of the Moon by infrared and microwave emissions and by radar. *Radio Sci.* **5**, 189–227.
- Hagfors, T., and J. V. Evans 1968. Radar studies of the Moon. In *Radar Astronomy* (J. V. Evans and T. Hagfors, Eds.), pp. 219–273, McGraw-Hill, New York.
- Hapke, B. W. 1981. Bidirectional reflectance spectroscopy I. Theory. *J. Geophys. Res.* **86**, 3039–3054.
- Hapke, B. W. 1984. Bidirectional reflectance spectroscopy III. Correction for macroscopic roughness. *Icarus* **59**, 41–59.
- Hapke, B. W. 1986. Bidirectional reflectance spectroscopy IV. The extinction coefficient and the opposition effect. *Icarus* **67**, 264–280.
- Hapke, B. 1990. Coherent backscatter and the radar characteristics of outer planet satellites. *Icarus* **88**, 407–417.
- Hapke, B. 1993. *Theory of Reflectance and Emittance Spectroscopy*. Cambridge Univ. Press, New York.
- Hapke, B. 1996. Are planetary regolith particles backscattering? Response to a paper by M. Mishchenko. *J. Quant. Spectrosc. Radiat. Trans.* **55**, 837–848.
- Hapke, B., R. Nelson, and W. Smythe 1993. The opposition effect of the Moon: The contribution of coherent backscatter. *Science* **260**, 509–511.
- Hapke, B., R. Nelson, and W. Smythe 1998. The opposition effect of the Moon: Coherent backscatter and shadow-hiding. *Icarus* **133**, 89–97.

- Hartman, B., and D. Domingue 1998. Scattering of light by individual particles and implications for models of planetary surfaces. *Icarus* **131**, 421–440.
- Helfenstein, P. 1988. The geological interpretation of photometric surface roughness. *Icarus* **73**, 462–481.
- Helfenstein, P., and J. Veverka 1987. Photometric properties of lunar terrains derived from Hapke's equation. *Icarus* **72**, 342–357.
- Helfenstein, P., and J. Veverka 1989. Physical characterization of asteroid surfaces from photometric analysis. In *Asteroids II* (R. Binzel, T. Gehrels, and M. Matthews, Eds.), pp. 557–593. Univ. of Arizona Press, Tucson.
- Helfenstein, P., U. A. Bonne, S. Stolovy, and J. Veverka 1991. Laboratory photometric measurements of particulate soils out to the very large phase angles. *Reports of Planet. Geol. and Geophys. Prog.—1990*, NASA Tech. Mem. 4300, pp. 280–282.
- Helfenstein, P., N. Currier, B. Clark, J. Veverka, M. Bell, R. Sullivan, J. Klemaszewski, R. Greeley, R. T. Pappalardo, J. W. Head III, T. Jones, K. Klaasen, K. Magee, P. Geissler, R. Greenberg, A. McEwen, C. Phillips, T. Colvin, M. Davies, T. Denk, G. Neukum, and M. J. S. Belton 1998. Galileo observations of Europa's opposition effect. *Icarus* **135**, 41–63.
- Helfenstein, P., J. Hillier, and J. Veverka 1999. The albedo dependence of particle phase functions. *Icarus*, submitted.
- Helfenstein, P., J. Veverka, and J. Hillier 1997. The lunar opposition effect: A test of alternative models. *Icarus* **128**, 2–14.
- Hillier, J., B. J. Buratti, and K. Hill 1999. Multispectral photometry of the Moon and absolute calibration of the Clementine UVVIS camera. *Icarus*, in press.
- Kattawar, G. W. 1975. A three-parameter analytic phase function for multiple scattering calculations. *J. Quant. Spectrosc. Radiat. Trans.* **15**, 839–849.
- Kaye, B. H. 1978. Specification of the ruggedness and/or texture of a fine particle profile by its fractal dimension. *Powder Technol.* **21**, 1–16.
- Kroupenno, N. N. 1972. Some characteristics of the Venus surface. *Icarus* **17**, 692–698.
- Kroupenno, N. N. 1973. Results of radar experiments performed on automatic stations Luna 16 and Luna 17. In *COSPAR Space Research XIII*, pp. 969–973. Akademie-Verlag, Berlin.
- Kroupenno, N. N., A. G. Balo, E. G. Ruzskii, V. A. Ladyghin, V. V. Cherkasov, and V. S. Formin 1975. Results of radar experiments performed aboard the Luna 19 and 20 automatic stations. In *COSPAR Space Research XV*, pp. 615–620. Akademie-Verlag, Berlin.
- Lumme, K., and E. Bowell 1981. Radiative transfer in the surfaces of atmosphereless bodies. I. Theory. *Astron. J.* **85**, 1694–1704.
- Lumme, K., H. Karttunen, and W. M. Irvine 1985. Roughness of the lunar soil. *Earth Moon Planets* **33**, 19–29.
- Mark, D. M., and P. B. Aronson 1984. Scale-dependent fractal dimensions of topographic surfaces: An empirical investigation with applications to geomorphology and computer mapping. *Math. Geol.* **16**, 671–683.
- McKay, D. S., R. M. Frulland, and G. H. Heiken 1974. Grain size and the evolution of lunar soils. *Proc. Lunar Sci. Conf. 5th*, 887–906.
- McKay, D. S., G. Heiken, A. Basu, G. Blanford, S. Simon, R. Reedy, B. M. French, and J. Papike 1991. The lunar regolith. In *The Lunar Sourcebook* (G. Heiken, D. T. Vaniman, and B. M. French, Eds.). Lunar and Planetary Institute, Houston.
- Mishchenko, M. I. 1992. The angular width of the coherent backscatter opposition effect: An application to icy outer planet satellites. *Astrophys. Space Sci.* **194**, 327–333.
- Mishchenko, M. I., and J. M. Dlugach 1992. Can weak localization of photons explain the opposition effect of Saturn's rings? *Mon. Not. R. Astron. Soc.* **254**, 15–18.
- Mishchenko, M. I., and J. M. Dlugach 1993. Coherent backscatter and the opposition effect for E-type asteroids. *Planet. Space Sci.* **41**, 173–181.
- Mitchell, J. K., L. G. Bromwell, W. D. Carrier, III, N. C. Costes, and R. F. Scott 1971. Soil mechanics experiment. In *Apollo 14—Preliminary Science Report*, NASA SP-272, pp. 87–108. NASA, Washington DC.
- Morris, R. V. 1978. The surface exposure (maturity) of lunar soils: Some concepts and I_s/FeO compilation. *Proc. Lunar Planet. Sci. Conf. 9th*, 2287–2297.
- Muhleman, D. O., W. E. Brown, Jr., and L. Davids 1968a. Radar reflectivity analysis, lunar surface electromagnetic properties, Part I. In *Surveyor 7 Preliminary Report*, NASA SP-173, pp. 181–186. NASA, Washington, DC.
- Muhleman, D. O., W. E. Brown, Jr., and L. Davids 1968b. Lunar surface electromagnetic properties: Radar reflectivity analysis. In *Surveyor 7 Mission Report, Part 2: Science Results*, JPL Tech. Rpt. 32-1264, pp. 209–220. Jet Propulsion Laboratory, Pasadena.
- Orford, J. D., and W. B. Whalley 1983. The use of fractal dimension to quantify the morphology of irregular-shaped particles. *Sedimentology* **30**, 665–668.
- Power, W. L., and T. E. Tullis 1991. Euclidean and fractal models for the description of rock surface roughness. *J. Geophys. Res.* **96**, 415–424.
- Shepard, M. K., and B. A. Campbell 1998. Shadows on a planetary surface and implications for photometric roughness. *Icarus* **134**, 279–291.
- Shepard, M. K., R. A. Brackett, and R. E. Arvidson 1995. Self-affine (fractal) topography: Surface parameterization and radar scattering. *J. Geophys. Res.* **100**, 11,709–11,718.
- Shkuratov, Yu. 1988. A diffraction mechanism of brightness opposition effect of surfaces with complicated structure. *Kinemat. i Fiz. Nebesn.* **4**, 33–39. [In Russian]
- Shkuratov, Yu. 1995. Fractoids and photometry of solid surfaces of celestial bodies. *Solar System Res.* **29**, 421–432.
- Shkuratov, Yu., and A. Ovcharenko 1998. The opposition effect: Theoretical model and laboratory measurements. *Solar System Res.* **32**, 276–286.
- Shkuratov, Yu., and D. G. Stankevich 1997. Brightness distribution over the lunar disk at zero phase angle. *Solar System Res.* **31**, 213–218.
- Shkuratov, Yu. G., M. A. Kreslavsky, A. A. Ovcharenko, D. G. Stankevich, E. S. Zubko, C. Pieters, and G. Arnold 1999. Opposition effect from Clementine data and mechanisms of backscatter. *Icarus* **141**, 132–155.
- Shoemaker, E. M., R. M. Batson, A. L. Bean, C. Conrad, Jr., D. Dahlem, E. N. Goddard, M. T. Hait, K. B. Larson, G. G. Schaber, D. L. Schleicher, D. L. Sutton, G. A. Swann, and A. C. Waters 1970. Preliminary geologic investigation of the Apollo 12 landing site. Part A Geology of the Apollo 12 landing site. In *Apollo 12 Preliminary Science Report*, pp. 113–182. NASA SP-235.
- Shorthill, R. W., J. M. Saari, F. E. Baird, and J. R. LeCompte 1969. Photometric properties of selected lunar features. NASA Contractor Report CR-1429.
- Simonelli, D. P., M. Wisz, A. Switala, D. Adinolfi, J. Veverka, P. C. Thomas, J. and P. Helfenstein 1998. Photometric properties of Phobos surface materials from Viking images. *Icarus* **131**, 52–77.
- Simpson, R. A., and G. L. Tyler 1982. Radar scaling laws for the lunar surface. *IEEE Trans. Antennas Propagat.* **AP-30**, 438–448.
- Swann, G. A., N. G. Bailey, R. B. Batson, R. E. Eggleton, M. H. Hait, H. E. Holt, K. B. Larson, M. C. McEwen, E. D. Mitchell, G. G. Schaber, J. P. Schafer, A. B. Shepard, R. L. Sutton, N. J. Trask, G. E. Ulrich, H. G. Wishire, and E. W. Wolfe 1971. Preliminary geologic investigations of the Apollo 14 landing site. In *Apollo 14—Preliminary Science Report*, NASA SP-272, pp. 39–85. NASA, Washington, DC.
- Thomas, P. C., D. Adinolfi, P. Helfenstein, D. Simonelli, and J. Veverka 1996. The surface of Deimos: Contribution of materials and processes to its unique appearance. *Icarus* **123**, 536–556.
- Turcotte, D. L. 1992. *Fractals and Chaos in Geology and Geophysics*. Cambridge Univ. Press, New York.
- Tyler, G. L., and H. T. Howard 1973. Dual-frequency bistatic radar investigations of the Moon with Apollos 14 and 15. *J. Geophys. Res.* **78**, 4852–4874.
- Verbiscer, A., and P. Helfenstein 1998. Reflectance spectroscopy of icy surfaces. In *Solar System Ices* (B. Schmitt, C. de Bergh, and M. Festou, Eds.), *Astrophys. Space Science Library*. Kluwer Academic, Dordrecht.